Effect of Flame Deformation of Downward Propagating Flames Induced by Laser Irradiation Method on its Combustion Instability

（レーザー照射法による管内下方伝播火炎の変形が燃焼不安定性におよぼす影響）

Effect of Flame Deformation of Downward Propagating Flames Induced by Laser Irradiation Method on its Combustion Instability

By

Nguyen Truong Gia Tri

Submitted to the Department of Mechanical and Space Engineering, Hokkaido University, Japan, in Partial Fulfillment of the Requirement for the Degree of Doctor of Philosophy in Mechanical and Space Engineering

January 2021

Abstract

Thermo-acoustic instabilities result from complex dynamic interactions between heat release fluctuation from flame and acoustic oscillation filed. Thermo-acoustic instabilities are often destructive to the operation of combustion systems and are major challenge in the development of lean premixed combustors with ultra-low emissions. Therefore, Numerous researches have been conducted to understand the mechanisms of the thermo-acoustic instabilities. Of these, a simple experiment to generate and study thermo-acoustic instabilities is a downward-propagating flame in an open-closed tube.

Flames propagating in tubes with specific structure can spontaneously produce acoustic oscillations. A parametric instability represented by corrugated flame is transitioned from a vibrating flat flame which is subjected to a primary acoustic instability. According to a theoretical velocity coupling, the variation of flame surface area during propagation in tubes is theoretically studied to show a proportional effect to the growth rate of thermo-acoustic instabilities. This effect can be studied more precisely if flame structure is actively controlled. In previous studies, a single CO_2 laser irradiation (*SLI*) method was extensively used to artificially control the flame shape. In this thesis, a double laser irradiation (*DLI*) method is developed based on the *SLI* setup. A single or a double cellular structure is formed when a flat flame is exposed to the *SLI* or *DLI,* respectively. As a spatially sinusoidal shape is formed, the cellular structure is characterized by the amplitude of the cell (a) and wavenumber (k) as a function of wavelength, $k = 2\pi/\lambda$. Consequently, at a given laminar burning velocity and using the same total laser power, different coupling parameter a and k of the cellular structures propagating under *SLI* and *DLI* would generate different thermo-acoustic responses. These responses can be comparatively examined to develop a more comprehensive criterion for the transition from primary acoustic instability to parametric instability. Hence, the structure of the laser-induced flames and their effect on the growth of acoustic pressure fluctuations are discussed to clarify the criteria of the transition from primary acoustic instability to parametric instability.

In Chapter 1, the nature and the physics of thermo-acoustic instability were briefly reviewed. In addition, the flame acoustic coupling in combustion tube were presented. Then, the objective and the scope of this study were introduced.

In Chapter 2, the experimental setup of the *SLI* and *DLI* how the laser beams are directed into the combustion tube were described. The properties and compositions of gas

mixtures were specified. Then the experimental procedure to obtain the flame propagation induce by laser irradiation and acoustic pressure fluctuation was revealed.

In Chapter 3, effect of flame surface area (as a function of a and k) of downward propagating flames induced by *SLI* and *DLI* on transition from primary acoustic instability to parametric instability was clarified. The effect was revealed through an experimental comparison on the criteria of transition to parametric instability of flame when it is exposed to *SLI* and *DLI*. The distance between two beams in the *DLI* setup is fixed at 18 mm. The results showed that the growth rate of primary acoustic instability during the propagation of the deformed flame is important to enhance the pressure fluctuation amplitude that further reaches the critical value for the transition to parametric instability. Furthermore, a linear relationship was found between the area of the deformed structure (irrespective of its dimension) and the corresponding growth rate of acoustic pressure fluctuation during the propagation of the deformed flame. Using the *DLI* method, the actual flame area, rather than $(ak)^2$ as mentioned in the velocity coupling, was found to be the factor that determines the growth rate under nonhomogeneous cell distribution.

In Chapter 4, the effect of geometric deformed structures induced by *DLI* on the growth rate thermo-acoustic instability was presented. The experiments were conducted at a given laser power and laminar burning velocity while the distance between the beams is varied from 12 mm to 21 mm with interval of 3 mm. When the beam separated distance was smaller than 18 mm, individual cell was merged together, the laser-induced structures were no longer in the form of sinusoidal shape as an overlapping region was emerged between two superimposed cells. This resulted a difference effect on growth rate of acoustic pressure with non-sinusoidal and sinusoidal structure. In fact, the appearance of curvature at overlapping region gave an effect that contributed to the growth rate of thermo-acoustic instability during the propagation of deformed flame. Therefore, relationship between the flame area and the growth rate acoustic pressure fluctuation was not linear as found in the experiments discussed in the chapter 3 where all the geometric structures of deformed flame are the sinusoidal shape. Based on that, the contribution of curvature effect is determined. The result found that curvature effect of overlapping region had limited contribution to the total growth rate of acoustic pressure. And the flame surface area of laser-induced flame is confirmed to be the factor control the growth rate of thermo-acoustic instability.

In Chapter 5, a summary of finding in the present study and conclusion were given.

Keywords: Parametric instability, Single laser irradiation, Double laser irradiation method, Flame structures, Diffusive-thermal instability

Thesis Supervisor: Osamu Fujita

Title: Professor

Acknowledgements

Firstly, I would like to express my deepest and sincere gratitude to my supervisor Prof. Osamu Fujita, Head of Laboratory of Space Utilization, Hokkaido University for providing me the greatest opportunity to pursue my Ph.D. I am grateful for his generous support in submitting my application for the University admission. During my time at the University, I am grateful for his guidance with continuous supports, motivations, great suggestions with his immense knowledge in all the time of my research.

I want to send an appreciation to Professor Nozomu Hashimoto. During my research, he gave me a lot of questions and suggestions that are valuable contributions to my research works as well as to the process of publishing my research paper. Besides that, I would like to thank Ms. Miho Taga for her kind and prompt assistance on stuffs related to my research. Especially, I also want to send my thankfulness to Dr. Ajit Kumar Dubey with his great support on the way publishing my research paper.

I would like to show my genuine gratitude to my Master course supervisor, Prof. Iman Kartolaksono Reksowardojo and my mentor Dr. Duong Hoang Long who brought me a great chance to have a very first encounter with Professor Osamu Fujita asking for a Ph.D. vacancy.

I wish to acknowledge the judge committee, Prof. Harunori Nagata, Prof. Nobuyuki Oshima, Prof. Nozomu Hashimoto and Prof. Osamu Fujita on my Ph.D degree evaluation and also on my midterm evaluations.

My sincere thanks go to all member of my lab in general and of my research group in specific for their help in conducting experiment and significant suggestions to my research work. I really appreciate to Dr. Chung Yong Ho, Mr. Koyama and Mr. Yusuke Konno who assisted me a lot when I first came to the University and during the beginning of my research. Particularly, I sincere thank my lab mate Dr. Guo Feng and Mr. Yu Xia for their encouragements and conversations not only about research, also the life in Japan.

As a Monbukagakusho scholar, I would like to thank Ministry of Education of Japanese Government (MEXT) for providing me financial support during my studying at Hokkaido University. I also thank all the staffs of E3 program, International Affairs Office of Engineering for their assistances related to my study at the University.

Finally, I dedicate my thesis work to my big caring, loving and supportive family for their unceasing encouragement, spiritually support and for everthing. Also, my deep appreciation goes to all my Viet friends inside and outside Vitenam and my best Japanese friend for their caring and unconditional supports during my life in Japan.

Table of Contents

List of Figures

List of Tables

Nomenclature

SLI	single laser irradiation
DLI	double laser irradiation
T_u	unburnt gas temperature
T_b	burnt gas temperature
ρ_u	unburnt gas density
ρ_b	burnt gas density
S_L	laminar burning velocity
U_u	unburnt gas flow velocity
U_b	burnt gas flow velocity
$1/\tau$	growth rate of acoustic pressure or instability
a	wavenumber of cellular structure
k	amplitude of cellular structure
Le	Lewis number
D_{th}	thermal diffusivity
D_m	mass diffusivity
ϕ	equivalent ratio of unburnt gas
p'	acoustic pressure fluctuation
$\dot{q}'$	heat release rate fluctuation
v	control volume
u	acoustic velocity
u_a	reduced acoustic velocity
U_a	acoustic velocity of unburnt gas
δ	flame thickness

D	combustion tube diameter
L	combustion tube length
c	sound speed
ε	acoustic energy
ω	angular frequency
Z	transfer function from pressure coupling
E	Activation energy
β	Zel'dovich number: dimensionless activation energy
R	gas constant
τ_t	reduced transit time
κ	gas expansion ratio
c_p	specific heat at constant pressure
c_v	specific heat at constant volume
M	Mach number
Tr	transfer function from velocity coupling
Fr	Froude number
Pr	Prandtl number
Ma	Markstein number
A_0	initial acoustic pressure amplitude
A	final acoustic pressure amplitude
$\bar{S}$	average flame surface area
$t_{concave}$	propagation period of concave structure
t_{convex}	propagation period of convex structure
S_b	beam separated distance in the *DLI* setup

Chapter 1: Introduction

In this chapter, the background and characteristics of thermo-acoustic instabilities research are included. Various types of instabilities of flame front in a combustion tube are reviewed in the following section. An introduction to the phenomena of thermo-acoustic instability is presented and is followed by a survey of thermo-acoustic instabilities work that carried out recently. Subsequently, the motivation from previous works lead to the objective of the current study.

1.1 Instabilities in premixed combustion

In many applications relating to power generation, heating and propulsion, continuous combustion processes are commonly presented. Examples include industrial burners, steam and gas turbines, waste generators, and jet and ramjet engines. Continuous combustion processes feature a wide range of dynamics. The potential couplings involve the unsteady components of acoustics, flame dynamics, and hydrodynamic flow stability can lead to resonant oscillations, even starting at small ones, that substantially grow large enough to alter the characteristics of the reacting flow in some particular ways. These phenomena are referred to as combustion instabilities.

In consideration of physical characteristics, combustion instability can be categorized into three groups, not entirely distinct:

- Darrieus–Landau hydrodynamic instability
- Thermo-diffusive instability
- Thermo-acoustic instability.

The first two groups are intrinsic instabilities of flame fronts. The third instability results from a coupling between a flame and the acoustic waves generated by an unsteady flame propagating in a combustion system [1]. The hydrodynamic instability and some

mechanisms of thermo-acoustic instability have their origin in the change of density through the flame front. They concern flame wrinkling on a wavelength greater than the flame thickness.

1.1.1 The Darrieus–Landau hydrodynamic instability

All premixed flames are unconditionally unstable to a hydrodynamic instability due to the thermal expansion of the gas through the flame. The instability was first reported independently by George Darrieus [3] and by Lev Landau [4] and is usually referred as the Darrieus–Landau instability, henceforth abbreviated D-L instability. The analysis behind the D-L instability considers a planar, premixed flame front as a hydrodynamic discontinuity of zero thickness subjected to very small perturbations.

D-L instability can be described by simple mechanisms involving the difference in density between the cold fresh gas and the hot burnt gas during the combustion process. The theory considers a planar, infinitesimally thin premixed flame front as sketched in Fig.1.1 assuming that transforms the fresh reactive mixture, at temperature and density T_u, ρ_u, into hot burnt gas at temperature and density T_b, ρ_b. The flame front propagates normal to itself at a constant laminar speed S_L relative to the cold unburnt gas. This arrangement is referred to one in which the unperturbed flame is stationary, so cold gas directs toward the flame front at speed $U_u = S_L$, and the hot gases leave the front at a velocity $U_b = S_L(\rho_u/\rho_b)$ because of thermal expansion. U_u and U_b are the normal velocities relative to the flame front. Since the product ρT is almost constant in subsonic premixed flames, the density ratio, ρ_u/ρ_b, is approximately the same order of magnitude to the temperature ratio T_u/T_b, and is typically in the range of 5 to 9 for standard hydrocarbon-air flames [1].

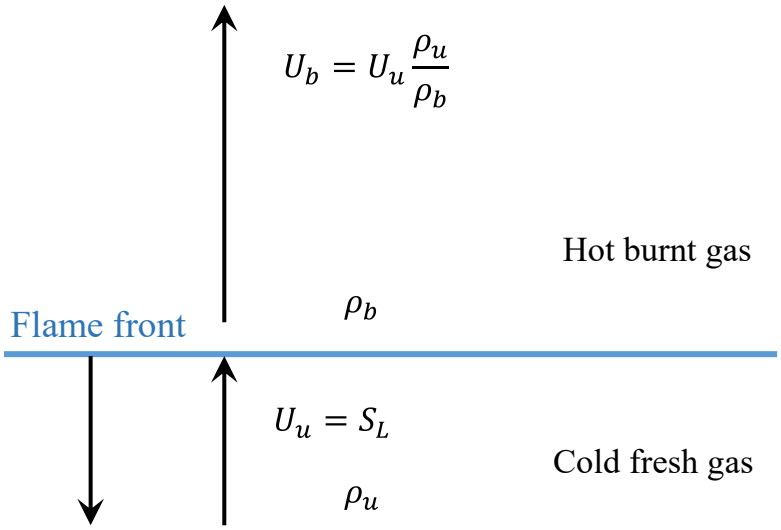

Fig. 1. 1. Gas velocities due to thermal gas expansion through a planar flame.

If the planar structure of flame is inclined, the situation shown in Fig. 1.1 is changed. Moreover, when the flame front is wrinkled the gas flow transport is more complicated. Consider now a situation shown in Fig 1. 2 where the flame is wrinkled at some wavelength λ and the upstream flows are curved, causing pressure gradients in the flow. The perturbations of the wrinkle are now nonlocal. The effect of gas expansion through a curved flame causes the flow to converge at places where the front is concave to the unburnt gas, and to diverge where the front is convex. Mass conservation implies that the upstream flow is accelerated (decelerated) at places where the flame front lags behind (is ahead of) the mean position. Since we have supposed that the propagation velocity of the front S_L is constant, the situation is unconditionally unstable.

Within this framework, dimensional analysis found that growth rate of the instability, $1/\tau$ is a function of the wavenumber k of the perturbation ($k = 2\pi/\lambda$, where λ is wavelength), flame speed S_L and the gas expansion ratio ρ_u/ρ_b. It is varied as [4]:

$$1/\tau = k.S_L.f(\rho_u/\rho_b) \tag{1.1}$$

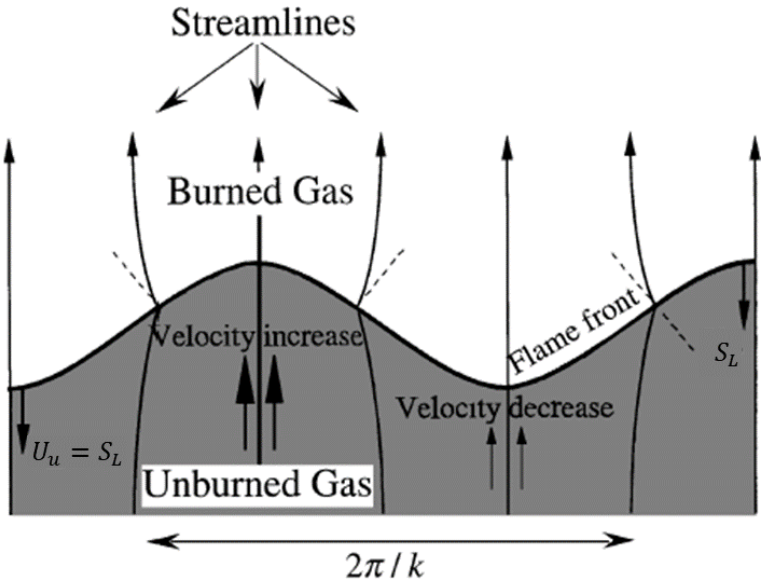

Fig. 1. 2. Curvature of flow lines through a wrinkled flame [5].

With $f(\rho_u/\rho_b)$ is positive function, the growth rate $1/\tau > 0$ for all wavenumber k, resulting in instability and the wrinkling will grow in time. Indeed, $1/\tau$ increases with increasing $f(\rho_u/\rho_b)$ and vanishing for $f(\rho_u/\rho_b) = 1$. In addition, from Eq. 1, the growth rate $1/\tau$ is proportional to k, implying that the wrinkling of short wavelength grows faster than the one of long wavelength. This expression is valid when the amplitude of wrinkling is small when compared with the wavelength.

The first direct experimental measurements of the growth rate of the D-L instability on a planar laminar premixed flame front was conducted by Christophe Clanet and Geoffrey Searby [6]. The intrinsically unstable flame is retained stable by a novel technique based on response of the flame to an acoustic parametric forcing before measurements. The growth rates of instability, calculated when the force is removed, are consistent with the theoretically predicted values. The growth of wrinkling of the cells initiated from a planar lean propane-air flame is clearly observed in Fig. 1. 3 after $140\ ms$ removing the parametric forcing.

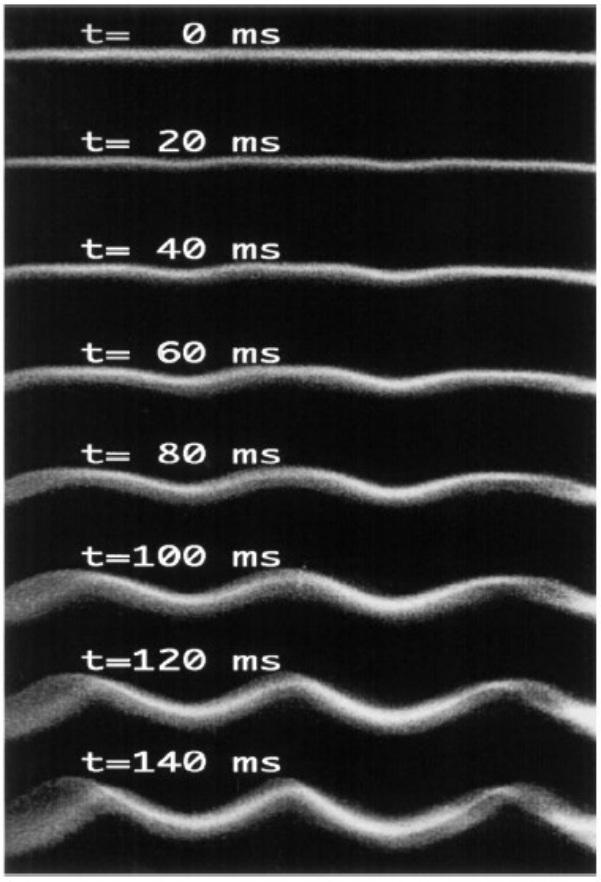

Fig. 1. 3. The temporal growth of D-L instability on an initially planar flame, the wavelength $2\ cm$, $S_L = 11.5\ cm/s$ [5].

1.1.2 Thermo-diffusive instability

When the wavenumber of wrinkling is much larger comparing to the flame thickness, the D-L instability mechanism cannot explain the growth of the wrinkling. The typical growth rate as a function of wavenumber is shown in Fig. 1. 4. In the case that the flame speed and the density change vary little, but the flame structure varies greatly or k is large, the principal features of the flame at large wavenumber cannot be understood on the basis of the instabilities far because. Other types of flame instability can occur independently of hydrodynamic effects and be explained the instability with high k named thermo-diffusive instabilities. They result from the competition between the molecular diffusion of species

and the conduction of heat. The ratio is represented by Lewis number, Le and specified as follow.

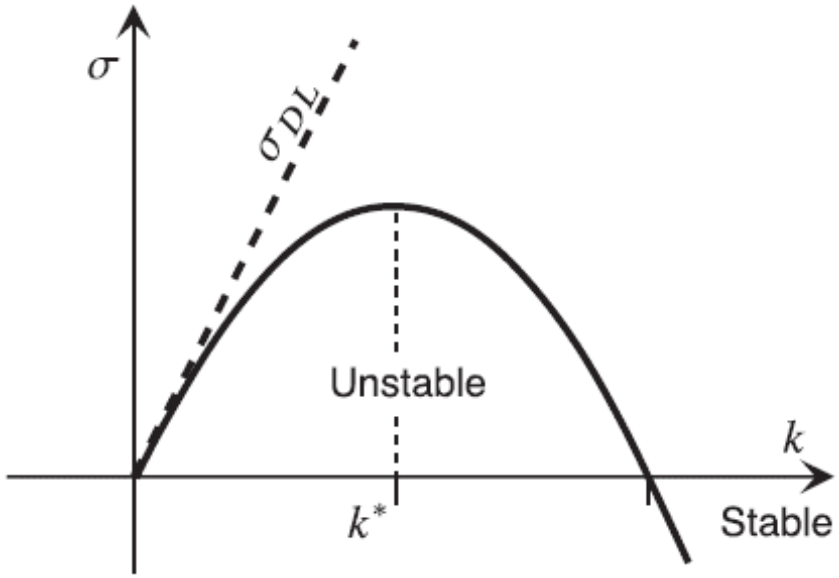

Fig. 1. 4. Growth rate as a function of wavenumber k [1].

Consider the front of a wrinkle flame perturbed from an initial planar flame, the structure now consists of alternating convex and concave structures toward the unburned mixture. In this framework, the gradients of temperature and species concentration are not normal to direction of propagation anymore, see Fig. 1.5 [6]. At the segment where the flame front is concave toward the unburnt gas, the heat fluxes (red arrows) are locally convergent result in an increase of local flame temperature and propagation velocity. The converse trend happens at the convex segment of the flame front that toward to the unburnt gas. In general, the thermal diffusion tends to stabilize the wrinkling. As a competitor to thermal diffusion, the effect of mass diffusion is in a direction opposite as illustrated as green arrow of mass flux in Fig. 1.5. At the segment where the flame front is concave toward the unburnt gas, the mass fluxes are locally divergent. The flux of reactive species into the reactive zone decreases,

resulting in a reduction in the local propagation velocity. The effect of the mass diffusion is to destabilize the wrinkled flame.

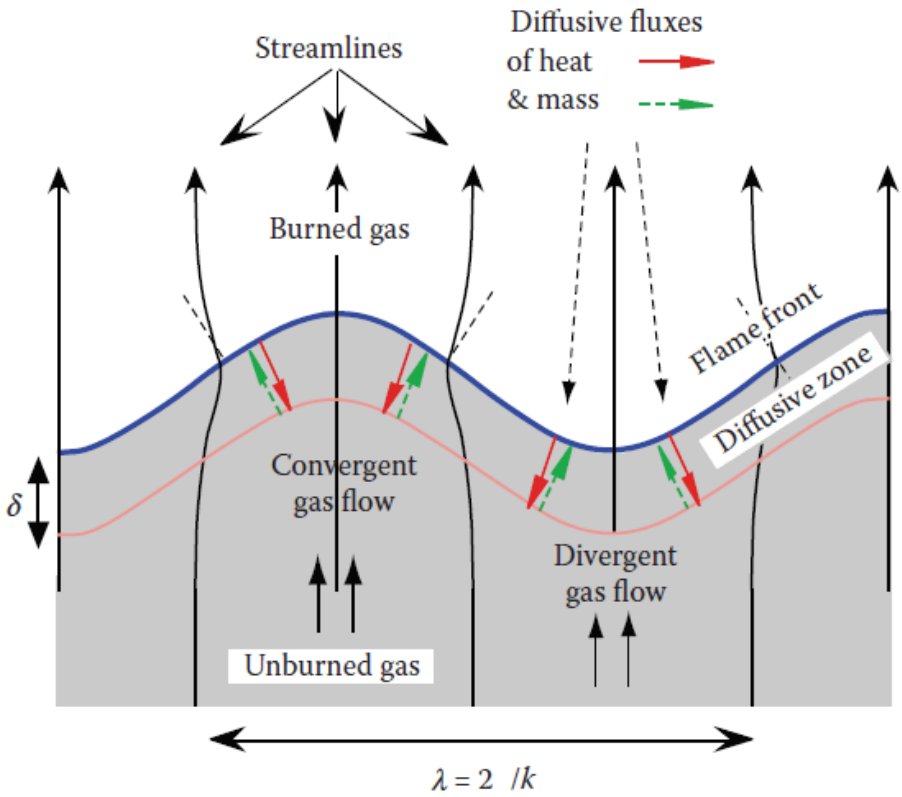

Fig. 1. 5. The diffusive transport at the internal structure of a wrinkled premixed flame.

For the latter, the wrinkling of flame front can be either facilitated or retarded will depend on the ratio of the thermal, D_{th}, and species, D_m, diffusion coefficient. This ratio is called the Lewis number.

$$Le = D_{th}/D_m \tag{1.2}$$

In general, when the wrinkling of the flame front occurs on a scale that wavenumber k is small compared with the flame thickness, the local modifications of flame structure are small compared with D-L instability effects. However, when k of wrinkling is larger than the flame thickness, the diffusive effects can dominate. The Lewis number is then an important factor in considering the growth of wrinkling. Specifically, if $Le > 1$, the burning

is intensified at the concave segment and weakened at the convex segment, leading to smoothing of the wrinkles. Consequently, such a flame is cellularly stable. With the same explanation, the converse holds for $Le > 1$ as the flame is cellularly unstable.

In summary, since the triggering of the diffusive-thermal instability, and the establishment of both the hydrodynamic and diffusional effect, are length-scale dependent as shown in Fig. 1. 4. An illustration of the flame subjected to the hydrodynamic and diffusive effect is shown Fig. 1.6 [1]. They are lean and rich propane-air flame having the same laminar flame speed, $S_L \approx 22.5\ cm/s$. The lean flame with a smaller wavenumber than the rich flame is affected by the hydrodynamic instability while the wavenumber observed on the wrinkles of rich flame is due to both hydrodynamic and diffusive instability.

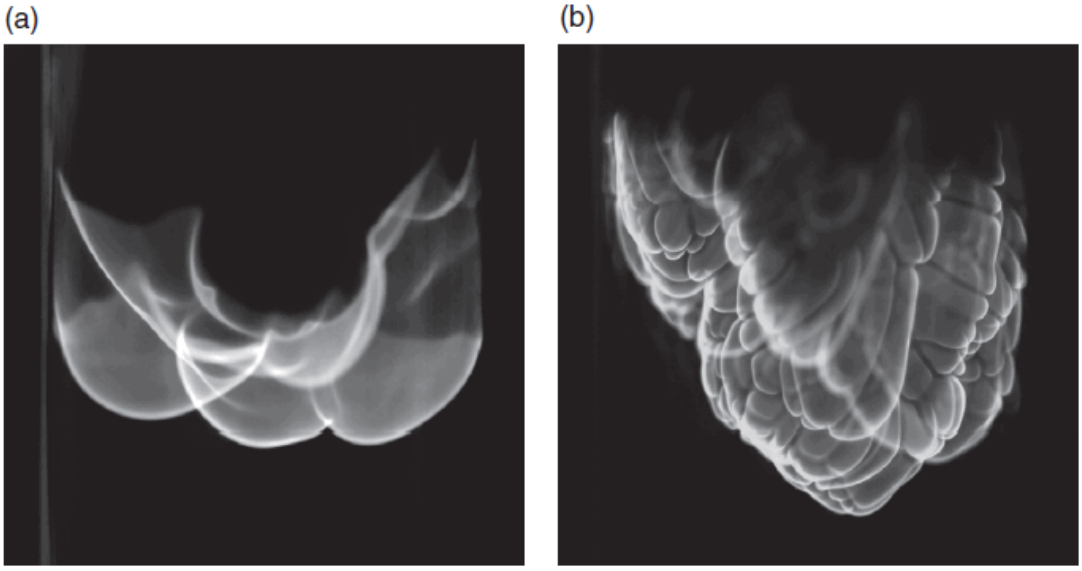

Fig. 1. 6. Propane-air flames in a 140 mm diameter of a combustion tube. (a) Lean flame, equivalence ratio, $\phi = 0.60$. (b) Rich flame, equivalence ratio, $\phi = 1.53$ [1].

1.1.3 Thermo-acoustic instability

In a typical continuous combustion process, a highly flammable fuel-air mixture is ignited, the chemical reaction happens releasing the hot burnt gases which are used to

perform certain functions. Combustion chambers can be viewed as organ pipes in which acoustic pressure and velocity oscillations can be sustained. Flames, which are essentially surfaces across which reactants are converted into products, not only possess their own intrinsic instabilities, but are also known to respond readily to periodically imposed fluctuations [7]. The feedback loop involves coupling of pressure and heat release rate oscillations can lead to thermo-acoustic instability. In this instability, the disturbances that enhance and change the characteristics of the flame are of an acoustic nature.

Historically, the first observation of thermo-acoustic instabilities was in laboratory experiments at the end of eighteen century. In 1777, Byron Higgins discovered the "singing flame" produced when a hydrogen diffusion flame stabilized at the exit of a burner is introduced into a tube [8]. The flame was found to excite the fundamental mode of the tube. The simplest example of a thermoacoustic instability is periodic sounds generated by an electrical heat source imposed in a given position of the Rijke tube as first observed by Rijke in 1859 [9].

Afterward, the instability was explained by Lord Rayleigh who describes the mechanism by which heat release could excite acoustic waves following a so-called Rayleigh criterion. The criterion was as follows: "If heat be periodically communicated to, and abstracted from, a mass of air vibrating in a cylinder bounded by a piston, the effect produced will depend upon the phase of the vibration at which the transfer of heat takes place. If heat be given to the air at the moment of greatest condensation or to be taken from it at the moment of greatest rarefaction, the vibration is encouraged. On the other hand, if heat be given at the moment of greatest rarefaction, or abstracted at the moment of greatest condensation, the vibration is discouraged". In more general terms, the Rayleigh criterion states that positive energy is transferred to the acoustic wave as the system is unstable if

there is a coupling mechanism that construct the pressure fluctuation and heat release fluctuation are in phase. This criterion is usually written in an integral form:

$$\int_0^v \int_0^{2\pi} p'\dot{q}' \mathrm{d}t\mathrm{d}v > 0 \tag{1.3}$$

where $p'$and $\dot{q}'$are the fluctuation of the pressure and the heat release rete, respectively. The integral is taken over the control volume of combustion, v, and over an acoustic cycle. Thermo-acoustic instability occurs when the inequality in Eq. (1) is satisfied.

Figure 1. 7 briefly outlines the conditions under which the thermo-acoustic is generated. The reactants enter on the left and the combustion products leaving on the right. The interaction between heat release through the flame and the acoustic modes of combustion system either adds or extracts the acoustic energy of acoustic oscillation. The judgment is followed the Rayleigh criterion. The sign of this integral is positive (negative) when this phase between the heat release and pressure fluctuations and difference is smaller (larger) than 90º. In addition, the system will be globally unstable if the acoustic gain is greater than the acoustic losses that are caused by radiation and convection of acoustic energy out of the system, viscous dissipation, and heat transfer. In general, combustion instabilities occur at frequencies associated with natural harmonic acoustic modes of the unsteady system.

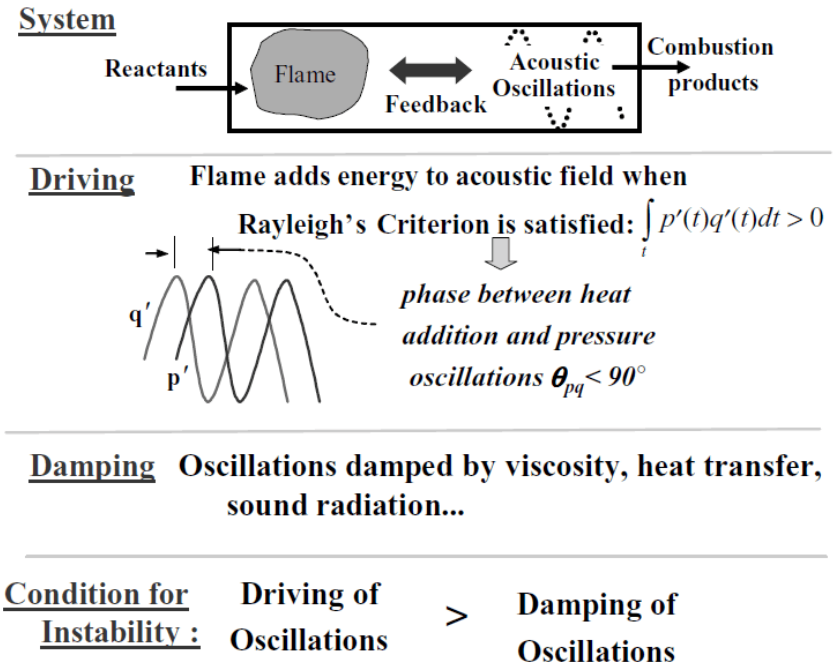

Fig. 1. 7. Summary of conditions required for a thermo-acoustic instability to occur [10].

In industrial application, thermo-acoustic instabilities are undesirable since, as observed in large scale engines, they are manifested by rising the heat release and pressure oscillations. These fluctuations lead to excessive vibrations resulting in engine failures, high levels of acoustic noise, high burn and heat transfer rates, and possibly component melting. Recently, the problem is becoming more relevant in the development of lean premixed combustion with high-power requirements and ultra-low emissions. The main challenge is to identify and describe the coupling mechanism of the acoustic wave and pressure wave. There are many possible mechanisms by which an acoustic wave can influence combustion. Possible coupling mechanisms include:

1. Direct sensitivity of the chemical reaction rate to the local pressure [11,12]
2. Oscillations of flame area induced by the acoustic acceleration [13,14]
3. Oscillations of total flame area induced by convective effects [15]
4. Periodic oscillations of the equivalence ratio in spray combustion [16,17]

The first and second mechanisms are more related to the work of current study which can used to explain the instabilities observed in a combustion tube. Accordingly, they will be discussed in the next sections.

1.2 Vibratory instability of downward-propagating flames in tubes

1.2.1 Observation of flame instabilities in tubes

In its simplest form, the combustion chamber can also be considered as a tube in which acoustic oscillations can be sustained. Additionally, longitudinal acoustic modes can be formed in the tube in which the acoustic energy is a sinusoidal function of the position of the tube. Accordingly, a downward-propagating flame interacts with a wide range of self-generated acoustic oscillations in the tube. At particular positions of the flame in the tube, the flame starts to oscillate and amplify the acoustic modes of the tube, then thermo-acoustic instabilities can be observed. The instabilities mechanism could be considered equivalent to thermo-acoustic instabilities mechanisms that may lead to strong discrete-frequency oscillations in combustion chambers of modern gas turbines.

Flames propagating in tubes can spontaneously produce acoustic oscillation. In a classical study of acoustic instabilities in a tube which has one open and another closed end, in 1992, Searby [18] has experimentally observed various acoustic instabilities under specific flame structures. They correspond to distinct phases of the spontaneous generation of acoustic oscillations produced by a premixed propane flame propagating in a tube as shown in Fig. 1. 8. Notice that, in the first half of the tube the flame has a curved shape generated by the D-L instability (see Fig. 1. 8a).

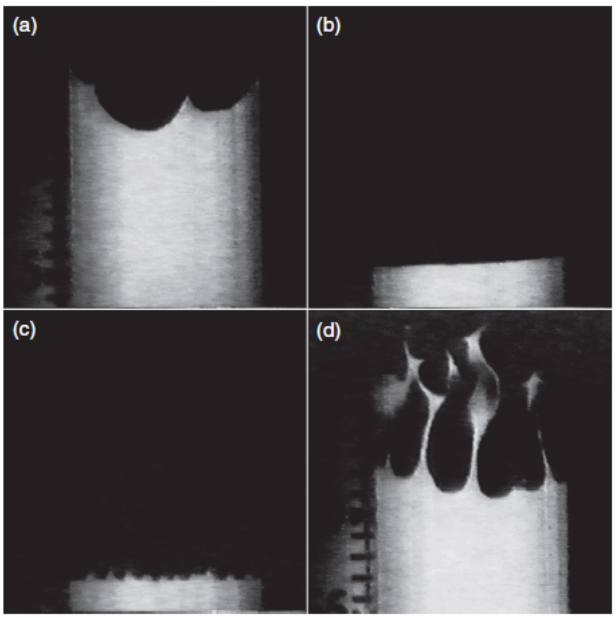

Fig. 1. 8. Tomographic cuts showing successive stages of a thermo-acoustic instability of a propane flame in a 10 cm diameter tube [1].

For a slow flame, a primary acoustic instability occurs corresponding to a flat flame oscillation. Specifically, the flat flame is stabilized by an oscillating acceleration filed which can suppress the initial D-L instability (see Fig. 1. 8b). As the flame speed increases, the primary acoustic instability rapidly transitions to violent secondary acoustic instability. At the onset of this instability, the flat flame becomes cellular with smaller corrugated cells oscillating at half of the acoustic excitation frequency (see Fig. 1. 8c). The wavenumbers of the corrugated structures and the acoustic velocity amplitude can be predicted using theoretical methods [14,19]. The secondary acoustic instability is accompanied by parametric instability producing a vibrating cellular flame and leading to turbulent flame (see Fig. 1. 8d). This parametric instability of the flame front is triggered only by pre-existing finite-amplitude acoustic oscillations [14]. At first few oscillating cycles of the parametric instability, the acoustic pressure grows rapidly to a peak, then decreases. An example of a

typical acoustic pressure recordings for a downward-propagating flame in a tube are shown Fig. 1. 9.

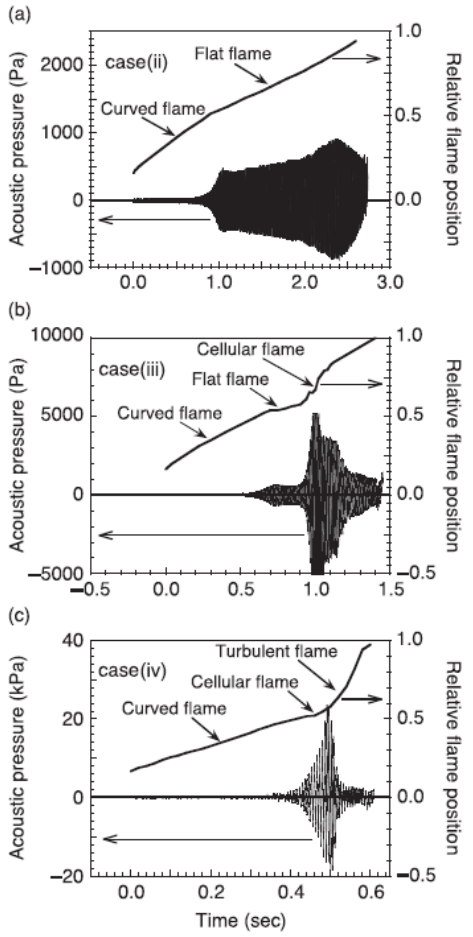

Fig. 1. 9. Recordings of acoustic pressure and flame position in a tube during thermo-acoustic for flame propagating in a tube of 120 cm long, 10 cm in diameter. (a) $S_L = 22\ cm/s$; (b) $S_L = 27\ cm/s$; (c) $S_L = 42\ cm/s$ [1].

In 1991, Searby and Rochwerger [14] conducted experimental and theoretical study on the parametric instability using laminar flame theory developed at that time. As a result, they have driven stability diagrams of downward-propagating flame. Fig. 1. 10 shows typical stability diagrams presented in the correlation of reduced acoustic velocity, $u_a = U_a/S_L$ and

reduced wavenumber of flame front, $k\delta = 2\pi\delta/\lambda$ (δ is flame thickness) under various values of the reduced frequency, the Markstein number, Ma, and the Froude number, Fr.

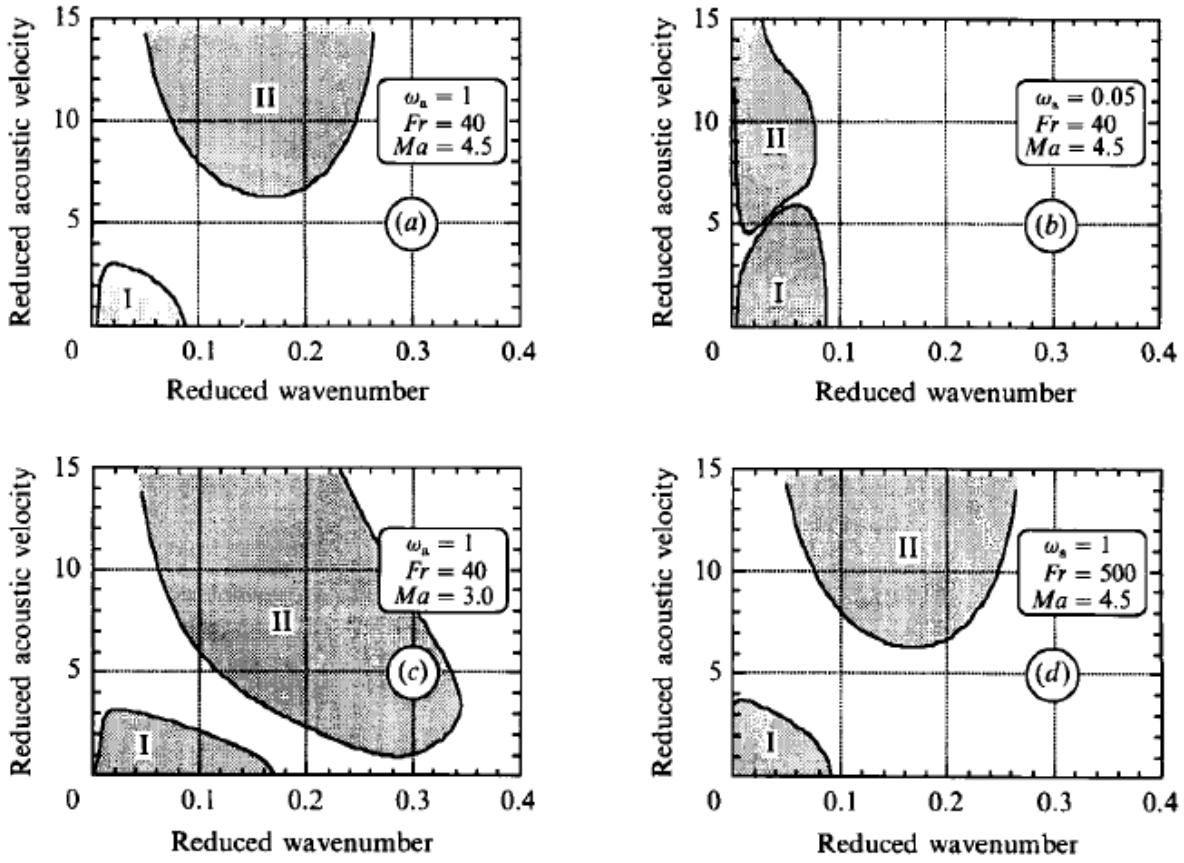

Fig. 1. 10. Stability diagrams of downward-propagating flames in tubes [14].

As shown in Fig. 1. 10, there are two distinct unstable regions of the flame instability, labelled I and II. The region I extends down to zero amplitude of acoustic excitation corresponding to the D-L instability. Similarity to the observation in the Searby experiments, the D-L instability can be re-stabilized by the oscillating acoustic acceleration and in general there exists a range of reduced acoustic velocities in which the planar flame is stable (see Fig 1. 10a). In the upper unstable region that is the domain of parametric instability, it is studied that at specific wavenumber of flame front, a corresponding acoustic velocity is needed to trigger this instability.

Based on the Rayleigh criterion. Several thermo-acoustic instability mechanisms have been proposed. They can be mainly classed into pressure coupling which considers the modifications of local internal structure and velocity coupling related to global geometry of the flame front.

1.2.2 Possible mechanism of flame and acoustic coupling in a combustion tube

Considering the Rayleigh criterion, when the hear release rate fluctuations from flame, $\delta\dot{q}$, and the pressure fluctuations, δp, are in phase, the order of magnitude of the linear growth rate is proportional to:

$$\frac{1}{\tau} \propto \frac{|\delta\dot{q}|}{|\delta p|} \tag{1.4}$$

Typically, the occupied ratio of flame front compared to the combustion zone in a tube is smaller than, or of the order of D/L, where D is the tube diameter and L is the tube length. For high aspect ratios ($L/D \gg 1$), the reaction zone can be treated as a discontinuity on the scale of the longitudinal acoustic mode. The mass conservation relation for the combustion process is given as follow:

$$\rho c^2(\nabla \cdot u) = \dot{q} \tag{1.5}$$

where ρ is the local gas density, c is sound speed and u is the acoustic velocity. After spatial integration over the combustion zone, the fluctuation amplitude of outgoing wave in the burnt gas is determined following a velocity jump in the gas velocity across the flame front as a discontinuity surface.

$$(\delta u_b - \delta u_u)\frac{\pi D^2}{4} = \iiint \frac{1}{\rho c^2}\delta\dot{q}\,\mathrm{d}^3 r \tag{1.6}$$

When the acoustic losses are neglected, the time derivative of the acoustic energy in the tube, ε, in the relation to the velocity jump is given by the expression:

$$\frac{\mathrm{d}\varepsilon}{\mathrm{d}t} = \delta p(\delta u_b - \delta u_u)\frac{\pi D^2}{4} \tag{1.7}$$

Evaluating ε in the form

$$\varepsilon \approx (\rho \delta u^2)\frac{\pi D^2}{4}L \approx \left(\frac{\delta u \delta p}{c}\right)\frac{\pi D^2}{4}L \approx \left(\frac{\delta u \delta p}{\omega}\right)\frac{\pi D^2}{4} \tag{1.8}$$

where ω is the angular frequency of the acoustic mode, from Eq. (1.7) and (1.8), the linear growth rate, $1/\tau$, can be defined as:

$$\frac{1}{\tau} = \frac{1}{\varepsilon}\frac{\mathrm{d}\varepsilon}{\mathrm{d}t} \approx \left(\frac{\delta u_b - \delta u_u}{\delta u}\right)\omega \tag{1.9}$$

Accordingly, the reduced growth rate is derived from Eq. (1.9) as follow:

$$\frac{1}{\omega\tau} \approx \frac{1}{\varepsilon}\frac{\mathrm{d}\varepsilon}{\mathrm{d}t} \approx \left(\frac{\delta u_b - \delta u_u}{\delta u}\right) \tag{1.10}$$

The transfer function characterizes the feedback mechanism of the acoustic wave on the flame front. For a pressure coupling, the transfer function, Z, in a temporal Fourier representation is given by:

$$(\delta u_b - \delta u_u) = Z\frac{\delta p}{\rho_u c_u} \tag{1.11}$$

where δu is positive towards the burnt gas that in the direction opposite to flame propagation. In the case of a planar flame, Clavin et al. [11] give an analytical expression for Z as a function of the acoustic frequency, reduced by the transit time through the laminar flame front, $\tau_t = D_{th}/S_L^2$, where D_{th} is the thermal diffusivity in the unburnt gas. For simplicity, they assumed that the combustion process takes place following a one-step reaction with a large activation energy, E, controlled by an Arrhenius law. Consequently, with a large activation energy, the chemical reaction occurs in a thin region, and Z is calculated as:

$$Z = \frac{\beta M}{2}\frac{T_b}{T_u}(\kappa - 1)N(\omega\tau_t), \tag{1.12}$$

where $\kappa = c_p/c_v$ is the specific heat ratio and β, the Zel'dovich number is the non-dimensional activation energy,

$$\beta = E(T_b - T_u)/(RT_b^2), \tag{1.13}$$

R is the gas constant, T_b and T_u are the temperature of the burnt and unburnt gases, M is the Mach number, $M = S_L/c$, and $N(\omega\tau_t)$ is a function of order unity depending on the inner structure of the flame. Eq. (1.10) and (1.11) show that the transfer function is also the order of magnitude of the linear growth rate:

$$\frac{1}{\omega\tau} \approx \frac{\beta M}{2}\frac{T_b}{T_u}(\kappa - 1), \tag{1.13}$$

The presence of the activation energy, β, shows that the instability results from a feedback through the temperature fluctuation in the acoustic wave. And because of large activation energy assumption, the change of heat release rate fluctuation is highly sensitive to the temperature oscillation. This was first noticed by Dunlap [20].

Pelce and Rochwerger [21] have derived a transfer function, Tr, to calculate the growth rate of an acoustic instability generated by the effect of an oscillating acceleration on the geometry of the flame front. They performed a linear analysis for a weak sinusoidal structure of flame front, $ak \ll 1$, where a is the amplitude and k is the wavenumber of the wrinkling. The analysis focused on a mechanism that the acoustic field can modulate the total surface area of the flame, leading to a modulation to the instantaneous heat release rate. If this acceleration is directed toward the burnt gas, then the amplitude of the cells will tend to decrease and inverse tendency holds for the acceleration that oriented toward the unburnt

gas. This is another possible coupling mechanism, called velocity coupling. This mechanism was first proposed by Rauschenbakh [22]. The transfer function Tr is given as follow:

$$Tr = \frac{(\delta u_b - \delta u_u)}{\delta u_u} \tag{1.13}$$

The results show that the transfer function is proportional to $(ak)^2$,

$$Tr = \frac{(ak)^2}{2}\left(\frac{\kappa}{\kappa - 1}\right) P(\omega\tau_t, k\delta), \tag{1.13}$$

where $k\delta$ is reduced wavenumber with $\delta = D_{th}/S_L$, $P(\omega\tau_t, k\delta)$ expresses the relative instantaneous perturbation to the amplitude of wrinkling of the flame.

It can be seen that the growth rate of pressure coupling is order of βM, $(M \ll 1)$ which is much smaller than that of velocity coupling is order of $(ak)^2$ (order of unity).

1.3 Motivation and objective of the study

1.3.1 Motivation of the study

Despite the fact that thermo-acoustic instabilities have been studied for long time ago, their control and elimination in practical combustion devices is still a problem that is difficult to master. A fundamental study on thermo-acoustic instability in general, the transition from primary acoustic instability to parametric instability in specific will be conducted in current work. Therefore, a lab-scale experiment to generate a downward-propagating flame in an open-closed tube is used.

Even though many works present parametric instability in propagating flame experiments, this instability has also been observed in burner stabilized premixed flames in tubes [14] . In principle, this instability can also occur in gas turbine combustion process if the amplitudes of existing oscillations are high enough for onset of parametric instability. In such cases, very high amplitude oscillations can be generated. These instabilities observed in the experiments of Searby [18] were also found in methane–air flames propagating

through the annulus of a Taylor–Couette burner [23,24]. Dubey et al. [25] analytically and experimentally studied the effect of geometric parameters on thermo-acoustic instabilities and found that velocity coupling mechanism is the dominant mechanism. However, pressure coupling can also be important when flame area does not change during flame propagation [26]. A critical diameter was also found at which the stronger parametric instability can be generated in mixtures with lowest laminar burning velocity [26]. The higher acoustic modes of the parametric instability can also be generated in gaseous fuels which has been experimentally and theoretically studied [27].

Essentially velocity coupling mechanism is related to the change in flame area which modulates the heat release to influence thermoacoustic instabilities. Pelce and Rochwerger [21] have theoretically derived a transfer function for velocity coupling mechanism used to define the growth rate of the thermo-acoustic instability driven by the acoustic acceleration of weak cellular flame front. Clanet et al. [28] extended the calculation for realistic flame, and the results were in good agreement to the results of experiment on propane–air flames with a higher aspect ratio, $ak \approx 0.5$. The effect of velocity coupling can be studied more precisely if we can control the flame structure. The big problem is that the propagating flame is usually intrinsic unstable, the wrinkled structure is not always regularly distributed and low spatial oriented as a wide range of wavenumber can be observed. Generally, the flame structure can be changed by changing the combustible mixture and geometry of the tube [26]. Another way is by modifying the flame shape artificially by irradiating the flame with a laser beam. In previous studies, the CO_2 laser irradiation method was extensively used to artificially control the flame shape. The laser energy, which is absorbed by the unburnt mixture, is negligible compared to the energy release of the flame. Hence, laser irradiation is used to generate specific deformed structures on the flame without significantly modifying

the mixture composition and properties. This method is a new experimental approach to study the interaction of flame structure and acoustic field.

For instance, a stability diagram is established based on the theoretical work of Searby and Rochwerger [14] for a premixed flame propagating in a tube as shown in Fig 1. 11. The flame is in a nearly planar shape and it cannot generate the transition from primary acoustic instability to parametric instability by itself. This condition corresponds to the yellow point in the diagram with a specific wavenumber and acoustic velocity. When the laser irradiation is applied, the flame is deformed to cellular structure with a given wavenumber, the condition of flame is now toward the red point as shown in the diagram. The structure variation induces an increment to the amplitude of acoustic velocity. Subsequently, with further increasing of acoustic velocity, it can reach the critical value of the upper region of parametric instability. This situation is marked as the red point at stability boundary of parametric instability region. Since the "pre-existing finite amplitude" of acoustic excitation is reached, the deformed cellular structure triggers the appearance of corrugated structure propagating at marginal wavenumber that is equivalent to the condition plotted as the blue point in the diagram.

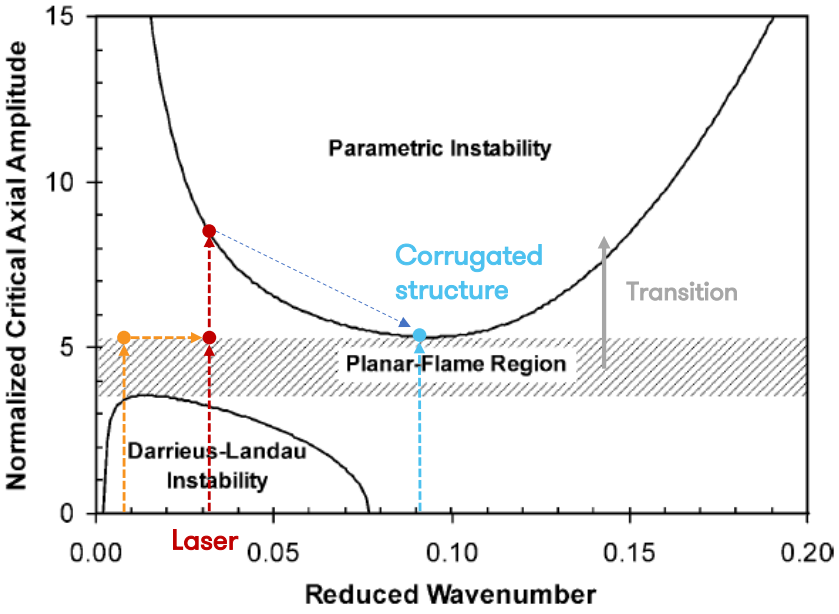

Fig. 1. 11. Understanding the transition to parametric instability with single laser irradiation.

With this advantage of laser irradiation, the method has been utilized to study the onset of primary acoustic instability [29,30], the effect of Lewis number on the generation of thermo-acoustic instability [31,32] and the mechanism of generation of parametric instability in a laser-irradiated flame [33,34]. Chung et al. [35] recently established a criteria map of the transition from primary acoustic instability to parametric instability when the flame curvature under different Le is controlled by external CO_2 laser irradiation. However, these studies use the single laser irradiation (*SLI*) method. When the flat flame is exposed to a single CO_2 laser beam, a single cellular structure is formed. It has limitation on controlling the range of deformed parameter a and k of cellular flame, a laser power results in a specific magnitude of a and k only.

In this work, we developed a double laser irradiation (*DLI*) method based on the *SLI* setup. *DLI* has a similar flame deformation process with that of the *SLI* setup but generates double cellular structures on the flame. As a spatially sinusoidal shape is formed, the geometry of the cellular structures is also characterized by the amplitude of the cell, a, and wavenumber, k. At a given S_L and using the same total laser power, *SLI* and *DLI* induce different coupling parameters for deformed cellular flames. Consequently, flames exposed to *SLI* and *DLI* generate different thermo-acoustic responses. These responses can be comparatively examined to develop a more comprehensive criterion for the transition from primary acoustic instability to parametric instability.

As shown in Fig 1. 11 how the single cellular structure induced the transition. Now without changing S_L and applying the same laser power, we can have another wavenumber, k with *DLI* and we can compare to the one obtained from single laser irradiation at the same diagram. The condition under *DLI* is represented by pink plots in Fig 1. 12. As can be seen in Fig 1. 12, wavenumber induced from *SLI* and *DLI* required different pre-existing finite

amplitudes of acoustic excitation, here is the critical acoustic velocity for parametric instability generation.

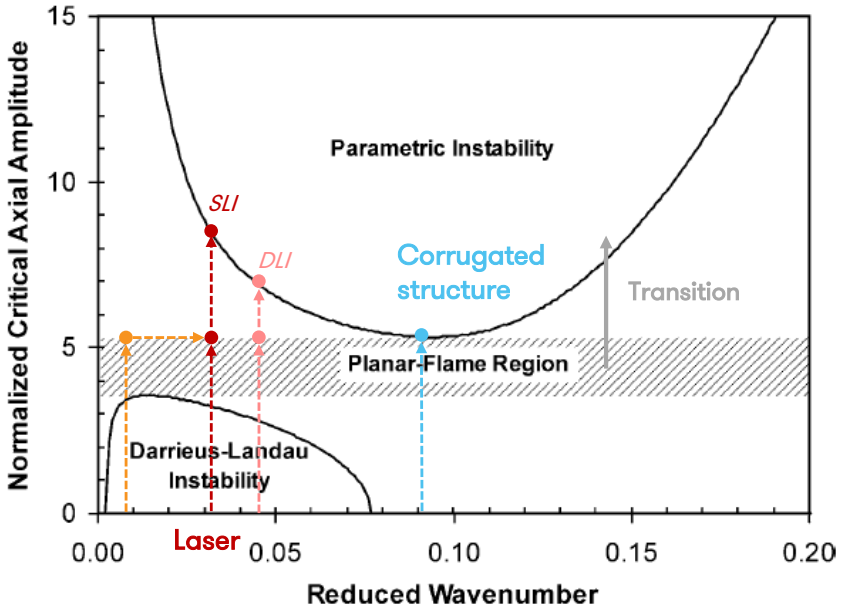

Fig. 1. 12. The transition to parametric instability with single and double laser irradiations.

1.1.4 Objective of the study

As mentioned above, with experiment using single and double laser irradiation, we can examine the effect of geometric parameter of deformed cellular flame on the transition from primary acoustic instability to parametric instability. In addition, with a wider range of a and k of deformed flame obtained from experiment on single and double laser irradiations, this work can provide an experimental validation for the theoretical velocity coupling in which the growth rate is described to be proportional to the coupling $(ak)^2$.

This work presents a comparative experimental investigation on downward-propagating flames exposed to *SLI* and *DLI*. The structure of the laser-induced flames and their effect on the growth of acoustic pressure fluctuations are discussed to clarify the criteria of the transition from primary acoustic instability to parametric instability. Parametric instability is one of the biggest problems that industrial application has been being dealing with to protect

combustor. Thus, understanding the transition mechanism will benefit for preventing that problem.

The experiments using *SLI* and *DLI* aim to flexibly control the shape of deformed flame. Using the same laser power, *SLI* and *DLI* can produce variety value of a and k for the conditions at which flames can derives the transition from primary acoustic instability to parametric instability. The criteria of the transition of laser-induced flames will be established. In addition, the flame structures and the corresponding time-dependent acoustic pressure of these deformed flame will be taking to account to clarify the transition mechanism. Then elucidating which factor dominantly govern the transition from primary acoustic instability to parametric instability.

Chapter 2: experimental setup and procedure

2.1 Experimental setup

The experiments were performed in a vertical combustion tube with setups of *SLI* and *DLI*, as shown in Fig. 2. 1. The combustion tube was a 705-mm-long transparent acrylic tube with a 50-mm inner diameter. The tube was open at the upper end and closed at the bottom end during experiments. A mechanism including electromagnets and springs was used to automatically open the top lid triggered by an external command at the beginning of ignition. $C_2H_4/O_2/CO_2$ mixture was filled into the tube through a small inlet with a valve. The effect of the Lewis number on the transition at $Le = 0.8$ and $Le = 1.05$ (treated as $Le > 1$) has been clarified in [35]. Thus, this study uses the same gas mixtures with $Le = 1.05$ used in [35]. The laminar burning velocity, S_L, of the gas mixtures was calculated using CHEMKIN (PREMIX) with a detailed chemical mechanism USC II [36].

Figure 2. 1 shows a schematic of both *SLI* (Fig. 2.1a) and *DLI* setups (Fig. 2.1b) and how they are guided into the combustion tube. The *SLI* setup included a CO_2 laser generator (SYNRAD Firestar v20; beam diameter, 3.3 mm; and wavelength, 10.6 mm), focusing lenses, a mechanical shutter, and a mirror (Mirror 1). The shutter was placed in the laser path to control the timing of laser irradiation. Two yellow ZnSe windows were attached to the top lid and bottom of the tube to enable the passing of the CO_2 laser beam(s) along and through the tube.

A CO_2 laser was used because it can be absorbed by C_2H_4 which presented in the test mixture [37]. The power of heat released from flame P_f is calculated as follow:

$$P_f = \Delta h\, \rho\, S_L\, A = c_p(T_b - T_u)\rho\, S_L\, A \tag{2.1}$$

where: ρ is unburnt mixture density (kg/m^3)

S_L is the laminar burning velocity (cm/s)

c_p is the specific heat of the unburnt mixture $(\mathrm{J/kg.K})$

T_u, T_b are the unburnt and adiabatic temperature (K)

A is the cross section area of flame, here the tube diameter is 5 cm

The power of laser absorption is compared to the power of heat released from flame. The calculation for P_f at $S_L = 13\ cm/s$ using in our experiment:

$$P_f = 885.19 \text{ x } (1820.48 - 298.15) \text{ x } 1.652 \text{ x } 0.13 \text{ x } \left[\pi \text{ x } \left(\frac{5}{2 \text{ x } 100}\right)^2\right] = 568.24\ (J/s)$$

The laser power absorbed by the unburnt mixture P_a is calculated as follow:

$$P_a = P_l[1 - exp(c\alpha S_L \Delta t)] \quad (2.2)$$

where: P_l is the laser power

α is absorption coefficient (1.5 $atm^{-1}\ cm^{-1}$), please refer the value to reference [34]

c is partial pressure of C_2H_4 which is the main absorption medium of CO_2 laser

Δt is the laser exposure time (s) ($S_L \Delta t$ is the propagation distance of flame during the laser exposure)

Here the calculation for laser power, $P_l = 12\ W$, then:

$$P_a = 12[1 - exp(0.05893 \text{ x } 1.5 \text{ x } 0.13 \text{ x } 3)] = 11.62\ (J/s)$$

It is understood that the laser power absorbed by the unburnt mixture is around 2 % of power of heat released from flame. Therefore, it is considered that the whole combustion process is not strongly affected by the laser power absorption while the laser irradiation is mainly used to generate local deformation of the flame. Accordingly, it is assumed that only the unburnt mixture absorbs the laser energy.

The *DLI* setup was configured by adding an optical arrangement to the *SLI* setup. The added arrangement consisted of a plate beam splitter and another mirror (Mirror 2). The beam splitter was set at a 45º angle to the incidence beam to separate it into a reflected and a transmitted beam at 50:50 ratio (tolerance of 3%). Mirror 2 was set below the beam splitter to fold the optical path of reflected laser beam by 90º making it parallel to the transmitted laser beam. Consequently, two spitted laser beams were collimated and then directed into the tube due to the normal reflection in mirror 1. The beam separated distance can be easily varied in the *DLI* experiments. Note that the only difference between the *DLI* and *SLI* setups was the additional optical arrangement. In the *DLI* experiment, the double laser beam was created by splitting the single laser beam from the *SLI* setup, making the results collected using the two setups comparable. Moreover, the power of the laser beam(s) from *SLI* and *DLI* was measured to ensure comparable results between *SLI* and *DLI* experiments.

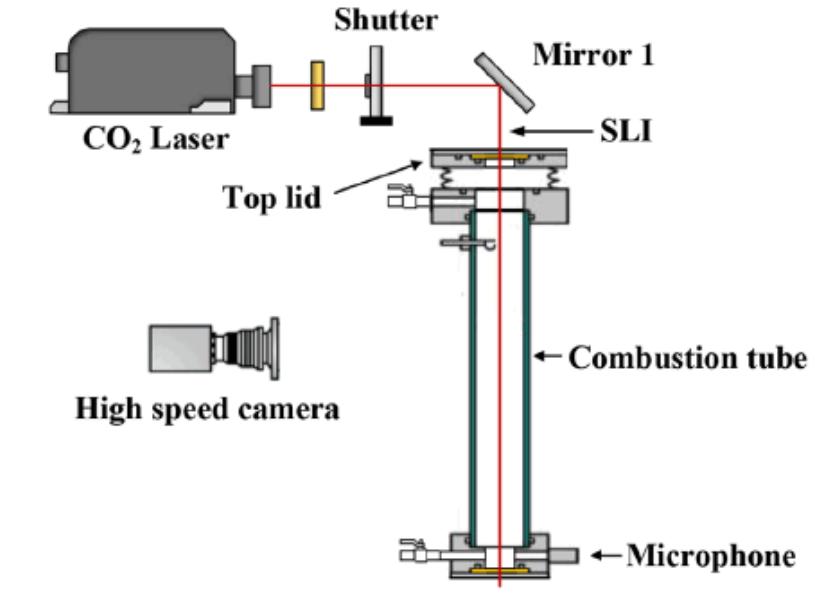

Fig. 2. 1a: Schematic of SLI setup

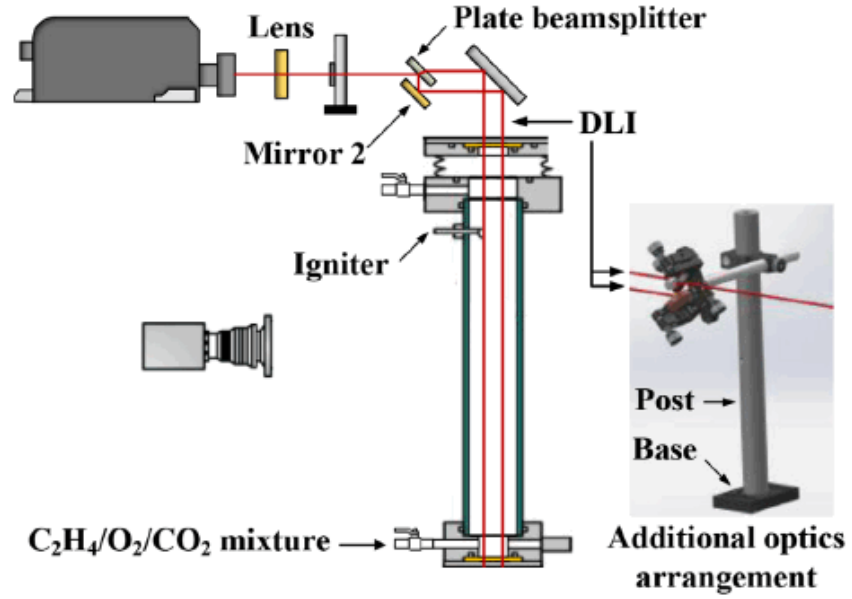

Fig. 2. 1a: Schematic of DLI setup

Fig. 2. 1. Schematics of the experimental setup.

2.2 Experimental procedure

In a typical experiment, the tube was flushed with premixed gases through a small hole that can be closed with a valve at atmospheric pressure and ambient temperature for few minutes while the top lid was closed. The valve was then closed, and the mixture was allowed to become uniformly quiescent. Consequently, the top lid was opened, and the mixture was immediately ignited by a spark plug installed near the top end of the tube. Hence, the combustion took place under one open end and another closed end boundary condition.

In this work, the experiments on the condition without using laser irradiation was firstly conducted to find the range of laminar burning velocity, S_L, where the laser irradiation could be applied. In the experiments using laser irradiation. the laser irradiation was started after ignition a certain time that was set initially by the shutter. The flame was then exposed to the laser irradiation. The flame was continuously exposed to laser irradiation for 3 s to allow the deformed structure to propagate through the middle region of the tube where maximum growth rate of thermo-acoustic instability is usually observed [21,25].

During the flame propagation. a high-speed camera (FASTCAM Mini UX100 recording at 1000 fps) was used to record the side-view of flame behavior. The pressure fluctuation of the unburnt mixture during flame propagation was measured by a pressure sensor (PCB Piezotronics) flush mounted at the bottom end. The maximum laser power used in this experiment was 12 W. The laser was irradiated 0.8 s after the ignition and slightly before the appearance of the flat flame in experiments. Each experimental condition was repeated at least six times and excellent reproducibility were observed. Here, a representative experiment for each case is presented. The setup of *SLI* and *DLI* were easily interchangeable, so the experimental conditions of *SLI* and *DLI* were done in turn in the same series of experiment. That enhanced the comparability of experimental results.

Chapter 3: Effect of surface area of laser-induced flame on transition to parametric instability

In this chapter, an introduction to the propagation phenomena and the cellular structures of flames induced from *SLI* and *DLI* experiments are introduced. Various types of instabilities observed in the experiment are reviewed. In the following section, the experiment results are classified based on the criteria of a transition from primary acoustic instability to parametric instability. Based on that, the investigation on the correlation between laser-induced flame and characteristics of thermo-acoustic instabilities is carried out. Specifically. the detailed analysis regarding to the effect of cellular structure and area of flames induced by *SLI* and *DLI* on the change in the acoustic pressure fluctuation during the propagation period of that deformed flames. Eventually, the mechanism of the transition from primary acoustic instability to parametric instability of laser-induced flames is clarified.

3.1 Observation of downward-propagating flame induced by the laser irradiation.

The experiment was done with mixture of C_2H_4 and O_2 diluted by CO_2 at $Le = 1.05$. Table 3. 1 lists the properties and compositions of gas mixtures. With experimental conditions using laser irradiation, the laser was irradiated 0.8 s after the ignition, which is slightly before the appearance of the flat flame in the initial period of the growth of the primary acoustic instability. In *DLI* experiment, the beam separation was fixed at 18 mm. The flame was continuously exposed to laser irradiation for 3 s to allow the deformed structure to propagate through the middle region of the tube where it gains the maximum growth rate of thermoacoustic instability.

Table 3. 1 Composition and properties of experimental gas mixtures with Le>1

C_2H_4 [%]	O_2 [%]	CO_2 [%]	ϕ	Le	S_L [cm/s]
5.445	20.418	74.137	0.8	1.05	10
5.893	22.098	72.009			13
6.007	22.525	71.468			14
6.119	22.945	70.936			15
6.232	23.334	70.434			16

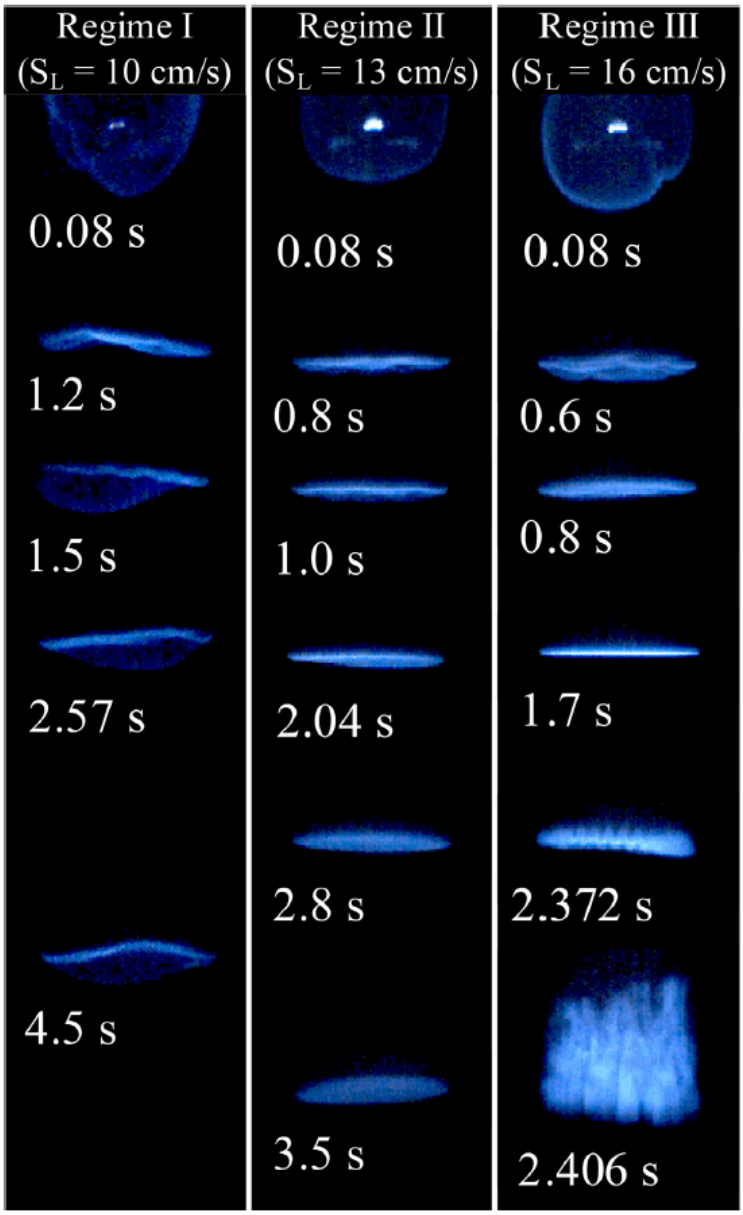

Fig. 3. 1. Still images of typical downward-propagating flame behaviors in the tube without laser irradiation (mixture compositions are given in Table 3. 1).

Figure 3. 1 shows three different regimes of downward-propagating flames without laser irradiation. The regime depends on laminar burning velocity, S_L. (I) For S_L below 11 cm/s, the flame propagates with a curved shape generated by hydrodynamic instability and produces no sound. (II) For S_L in the range of 12–15 cm/s, a vibrating flat flame developed from the initial curved flame propagating until the bottom of the tube in an acoustic field generated by the primary acoustic instability. (III) For S_L above 15 cm/s, parametric instability follows the primary acoustic instability. Parametric instability is triggered by a presence of the corrugated structures on the flat flame. The structure grows in amplitude for few cycles of fluctuation and eventually breaks into turbulent flame. These regimes are qualitatively similar to those reported in the previous work [18].

Thereafter, the flat flame in regime II where transition to parametric instability could not spontaneously occur was selected as the default flame for experiments with CO_2 laser irradiation. The laser could help the flat flame in regime II to generate a transition to parametric instability as in regime III but without increasing S_L. Due to the constant structure and surface area, the flat part that remained after laser irradiation had a limited contribution to the transition. Hence, the instability increment compared to that without laser irradiation is attributed to the propagation behavior of the deformed part of the flame. This consideration enables a clear description of the effect of laser irradiation on the transition criteria.

Figure 3. 2 presents the experimental flame images depicting sequential behaviors of the default flames induced by *SLI* and *DLI*. In general, the flame behaviors induced by *SLI* and *DLI* are qualitatively similar. Figure 3. 3 illustrates the flame deformation process for *DLI* case for easier understanding. Figure 3. 4 shows the pressure fluctuation associated with the conditions shown in Fig. 3. 2. Chung et al. [35] described the deformation of flames and their transition to parametric instability induced by *SLI*. Following the incidence of the laser beam, a portion of the unburnt mixture just before the flame front was preheated along the

laser path. As a result, the flame temperature was locally increased and the local burning velocity was downwardly enhanced at the center of the flame. The flame front was then deformed toward the unburnt mixture and formed a convex structure. Consequently, the thermal-diffusive effect comes into play as the gradient of temperature and species concentration is no longer parallel to the average direction of flame propagation. For a flame with $Le > 1$, due to the dominance of thermal diffusion over species diffusion, the convex flame front tends to be stabilized. Thus, the transition to parametric instability from the convex flame requires a higher laser power compared with the flame with a lower Le. On the other hand, the laser irradiation simultaneously decreases the density of the unburnt mixture along the laser path and causing a generation of upward flow induced by the buoyancy effect. With a laser exposure of 3 s, the strength of buoyancy-driven flow becomes significant and overcomes the evolution of the convex structure to a concave structure. This deformed concave flame continues to propagate and generates the transition to parametric instability with sufficient laser power. On the other hand, concave structure formation has been previously described in [38].

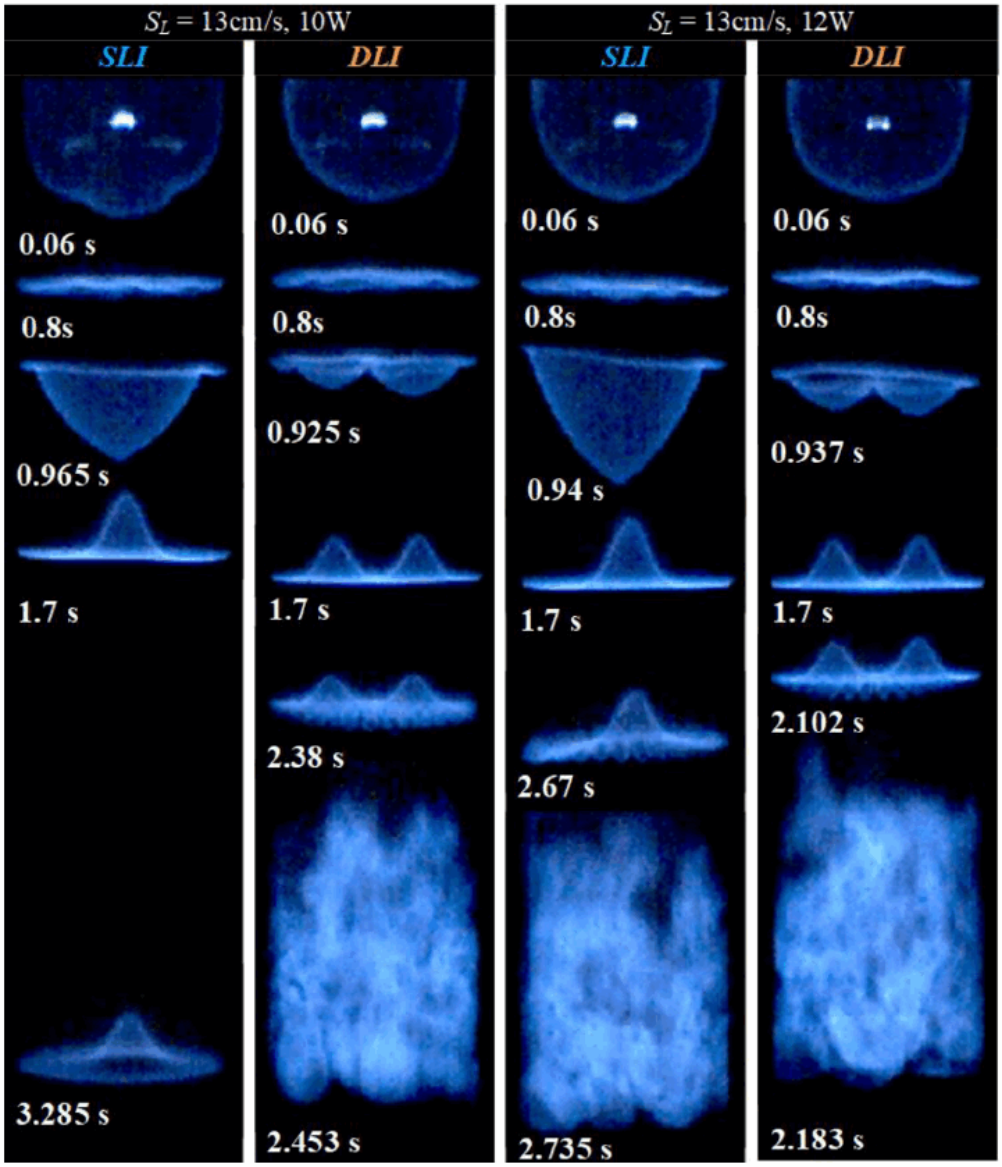

Fig. 3. 2. Flame propagation behavior induced by *SLI* and *DLI* under various total laser powers (mixture compositions are given in Table 3. 1).

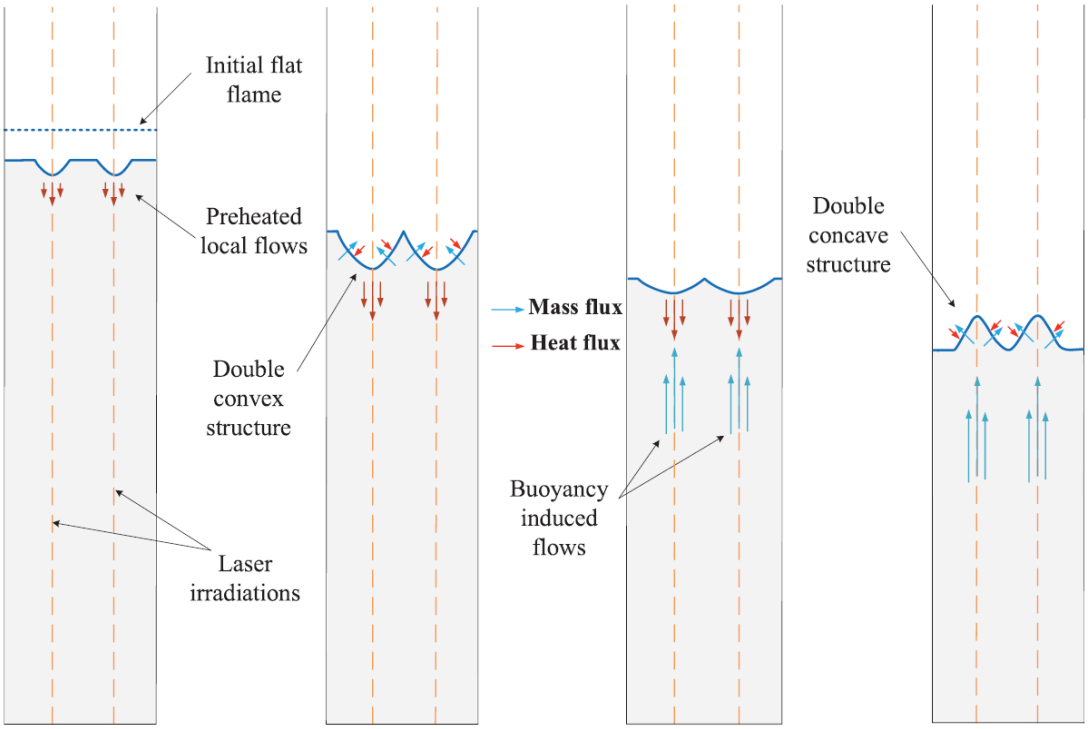

Fig. 3. 3. An illustration of the concave structure deformation process of the flame induced by *DLI*.

From Fig. 3. 3, it can be seen that the double concave structure was developed from the initial double convex structure along the two laser paths, and it further initiated the transition at a critical laser power. As described above, a large single cellular structure or a smaller double concave structure can be artificially induced from the flat flame using *SLI* or *DLI* at the same total laser power. It can be seen that the amplitude of the concave structure is lower with *DLI* than that with *SLI* because the amount of energy added by laser heating is halved for each beam at the same total laser power. As shown in Fig. 3. 2, 10 W of laser power used in the *SLI* setup cannot drive the transition to parametric instability, but it does in the case of *DLI*. Therefore, various flame structures or variety of geometric parameter a and $k$induced by *SLI* and *DLI* methods lead to a difference in critical laser power at which the transition occurs. Clearly, the total laser power is not the criterion to generate the transition to

parametric instability from a flat flame, and flame dynamics generated by *SLI* and *DLI* needs to be further clarified. The transition from primary acoustic instability to parametric instability is recognized by the onset of the corrugated structure and followed by a sudden increase in the amplitude of acoustic pressure compared to that in the primary acoustic instability region as shown in Fig. 3. 4. Most of conditions shown in Fig. 3. 4 demonstrated this sudden acoustic pressure increment in the parametric instability region, except for the case of *SLI* at $S_L = 13\ \mathrm{cm/s}, 10\ \mathrm{W}$ laser power.

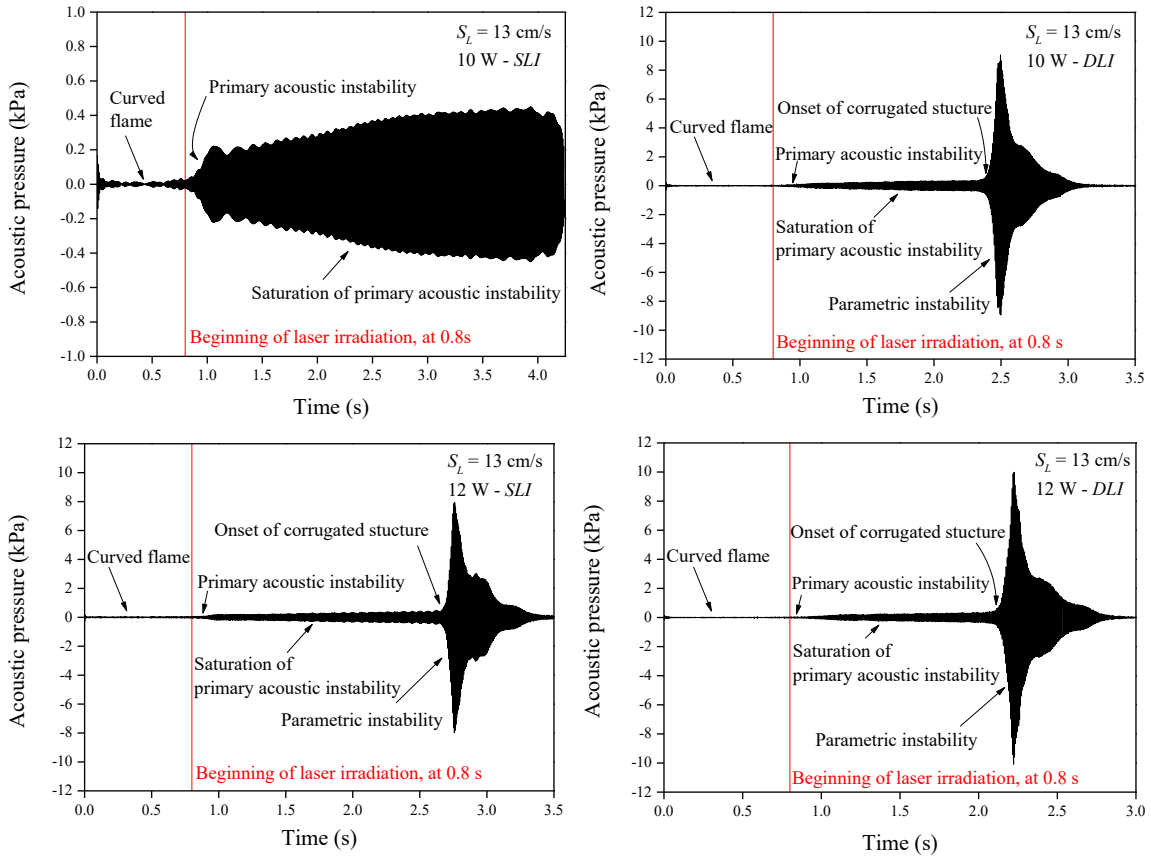

Fig. 3. 4. Pressure fluctuations of the conditions shown in Fig. 3. 2.

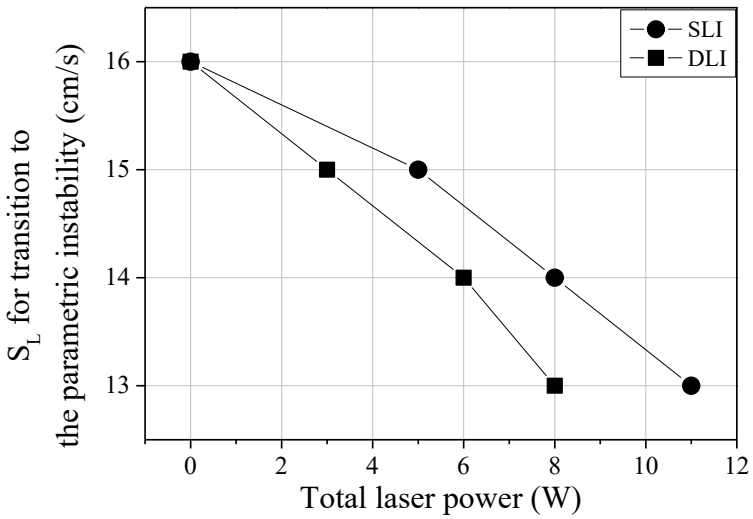

Fig. 3. 5. Critical laser power required for the transition under various laminar burning velocities (mixture compositions are given in Table 3. 1).

Figure 3. 5 shows critical laser power, which is the minimum total laser power required to induce the transition to parametric instability from the flat flame for a range of S_L from 13 cm/s to 16 cm/s. For *DLI*, the horizontal axis denotes the total power of the two laser beams in the *DLI* setup or the power of a single beam in the *SLI* case. At $S_L = 16\ cm/s$, transition occurs without laser irradiation (i.e., the critical laser power is $0\ W$). When $S_L < 16\ cm/s$, transition occurs only with laser irradiation for the deformed concave flame. Figure 3. 5 shows that the minimum laser power required for generating the transition of the flame reduces as S_L increases which is understandable because by increasing S_L we are moving closer to the onset of regime III where parametric instability is generated without any laser irradiation. Importantly, at a given S_L, *DLI* triggered the transition using a lower laser power compared to *SLI*. This result indicates that the flame deformation by *DLI* is more effective than that by *SLI* in causing the transition from primary acoustic instability to parametric instability at the same total laser power. Consequently, the flame structure and pressure

history generated by the *SLI* and *DLI* were further analyzed to understand the factors controlling the transition to parametric instability.

3.2 Correlation between the experimental result and theoretical velocity coupling mechanism

Searby and Rochwerger [14] presented a theoretical stability diagram for the transition from a flat flame to parametric instability in an acoustic field. They have shown that when the acoustic velocity or pressure fluctuation amplitude reaches a critical value, parametric instability is generated at a certain wavenumber of the corrugated structure (at the onset of the transition, as shown in Fig. 3. 2). The stability diagram can be established by Mathieu's equation [14], which represents a parametric oscillator and is given as follow:

$$\frac{d^2Y(z)}{dt^2} + [a - 2q\cos(2z)]Y(z) = 0 \tag{3.1}$$

Here, $z = \frac{1}{2}\omega_a t$; $a = \frac{4AC_0 - B^2}{\omega_a^2 A^2}$ and $q = \frac{2C_1}{\omega_a^2 A}$. The analytical functions are defined as:

$$A = (2-\gamma) + \gamma k\left(Ma - \frac{J}{\gamma}\right) \tag{3.2}$$

$$B = 2k + 2\frac{k^2}{1-\gamma}(Ma - J) \tag{3.3}$$

$$C_0 = \frac{\gamma k}{Fr}\left[1 - k\left(Ma - \frac{J}{\gamma}\right)\right] \tag{3.3}$$

$$-\frac{\gamma}{1-\gamma}\left\{k^2 - k^3\left[h_2 + \frac{\gamma+2}{\gamma}Ma - \frac{2J}{\gamma} + (2Pr-1)\int_0^1 (h_2 - h(\theta)d\theta)\right]\right\}$$

$$C_1 = \gamma k\omega_a u_a\left[1 - k\left(Ma - \frac{J}{\gamma}\right)\right] \tag{3.4}$$

where, $\gamma = \frac{\rho_u - \rho_b}{\rho_u}$ is the normalized gas expansion coefficient, k in these functions is the wavenumber normalized by the flame thickness ($\delta = D_{th}/S_L$ where D_{th} is the thermal diffusivity in the unburnt gas). $Fr = \frac{S_L}{g\delta}$ is Froude number (g is gravitational acceleration).

Pr is Prandtl number. $\omega_a = \omega\tau_t$ is the reduced acoustic angular frequency from the one obtained from experiments normalized by flame transit time, τ_t. $u_a = U_a/S_L$ is the reduced acoustic velocity, where U_a is the acoustic velocity of the unburnt gas. $\theta = \frac{T-T_1}{T_2-T}$, is the normalized temperature, $h(\theta) = \frac{(\rho D_{th})_\theta}{(\rho D_{th})_{\theta=0}}$, $h_2(\theta)$ is $h(\theta)$ in the burnt gas. When $h(\theta)$ is known for a mixture, following integrals can be computed:

$$J = \frac{\gamma}{1-\gamma}\int_0^1 \frac{h(\theta)}{1+\theta\frac{\gamma}{1-\gamma}}\mathrm{d}\theta \tag{3.5}$$

And Ma is the dimensionless Markstein number defined as:

$$Ma = \frac{J}{\gamma} - \frac{1}{2}\beta(Le-1)\int_0^1 \frac{h(\theta)ln(\theta)}{1+\theta\frac{\gamma}{1-\gamma}}\mathrm{d}\theta \tag{3.6}$$

A stability solution of Eq. 3.1 may be written in the form [39]

$$Y(z) = e^{i\mu z}\sum_{k=-\infty}^{+\infty} P_{2k}e^{i2kz} \tag{3.7}$$

For $Y(z)$ to be a solution of Mathieu's equation, the variable μ should satisfy the following equation [40]

$$\cos(\pi\mu) = 1 - \Delta(0,a,q)\left(1-\cos\left(\pi\sqrt{a}\right)\right) \tag{3.8}$$

For an arbitrary r, $\Delta(0,a,q,r)$ is given by following tridiagonal matrix:

$$\begin{vmatrix}
1 & l_{2r} & \cdots & & & & & & \\
l_{2(r-1)} & 1 & l_{2(r-1)} & & & & & & \\
\vdots & \vdots & \ddots & & & & & & \\
 & & l_{-2} & 1 & l_{-2} & & & & \\
 & & & l_0 & 1 & l_0 & & & \\
 & & & & l_2 & 1 & l_2 & & \\
 & & & & & & \ddots & & \\
 & & & & & & l_{2(r-1)} & 1 & l_{2(r-1)} \\
 & & & & & & & l_{2r} & 1
\end{vmatrix} \tag{3.9}$$

With $l_{2r} = \frac{q}{(2r-i\mu)^2-a}$. $\Delta(0,a,q)$ can be found by setting $\mu = 0$ in above matrix. And in this case l_{2r} turns to an even function, i.e., $l_{2r} = l_{-2}$ and so on. This matrix is an infinite matrix as r is ∞. Fortunately, the matrix can be calculated by a three-point recursive formula suggested by Strang [41].

$$\Delta(0,a,q,r) = n_{2r}\Delta(0,a,q,r-1) - m_{2r}n_{2r}\Delta(0,a,q,r-2) + m_{2r}m_{2(r-1)}^2\Delta(0,a,q,r-3) \tag{3.10}$$

Here, $m_{2r} = l_{2r}l_{2(r-1)}$, and $n_{2r} = 1 - m_{2r}$. The value of r should be large enough to find a good estimate of $\Delta(0,a,q)$. In practice, a converged value is obtained for small value of r. In this work we use $r = 20$. Once, $\Delta(0,a,q)$ is obtained, the stability factor F of the solution can be calculated as:

$$F = \frac{1}{\pi}\text{acosh}\left[1 - \Delta(0,a,q)\left(1 - \cos\left(\pi\sqrt{a}\right)\right)\right] - \frac{B}{A\omega_a} \tag{3.11}$$

The condition for marginal stability is given by $F = 0$. For a given wavenumber k and acoustic forcing u_a, the system is stable or unstable F is negative or positive. The stability boundary can be obtained in $k - u_a$ plane.

In this work, a similar stability diagram was calculated for the flat flame at $S_L = 16\ cm/s$, as shown in Fig. 3. 6. The horizontal axis is the reduced wavenumber, $\delta = 0.0082\ cm$. The vertical axis is the reduced acoustic velocity.

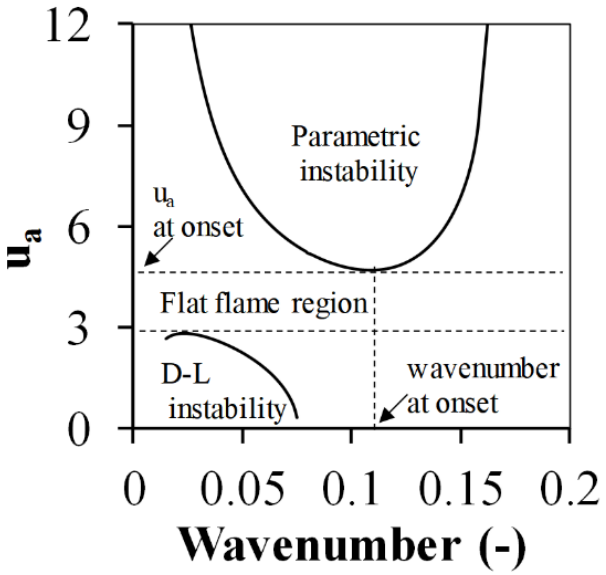

Fig. 3. 6. Stability diagram at $S_L = 16\ cm/s$ for $C_2H_4/O_2/CO_2$ mixture with $Le = 1.05$.

The measured wavenumber (see flame in Regime III at $t = 2.372\ s$ from Fig. 3. 1) of the corrugated structure at the onset of the parametric instability, $k\delta = 0.116$, is close to the value shown in Fig. 3. 6. With this understanding, the acoustic pressure fluctuation during laser-induced flame propagation is reviewed. Flames at $S_L = 13\ cm/s$ under critical laser powers of *SLI* –11 W and *DLI* –8 W are taken as a typical representation for conditions causing the transition by laser irradiation (transition conditions). These representative conditions are compared with the transition without laser irradiation at $S_L = 16\ cm/s$ and other non-transition conditions ($S_L = 13\ cm/s$, *DLI* –7 W and $S_L = 13\ cm/s$, 0 W without laser irradiation).

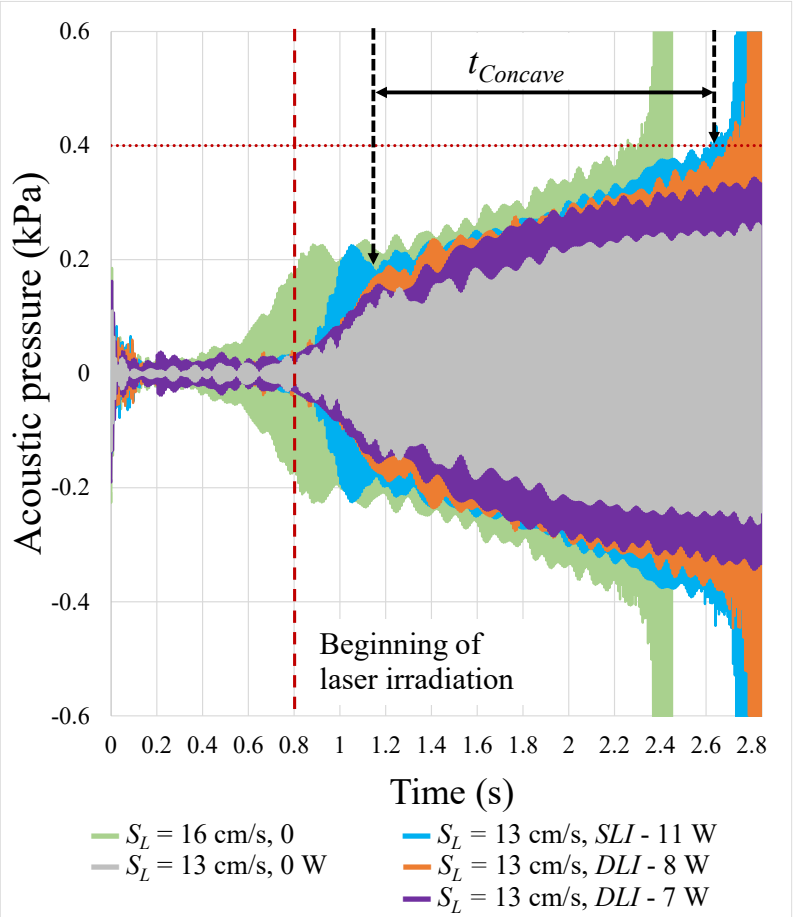

Fig. 3. 7. Acoustic pressure fluctuation in the tube during flame propagation under various conditions (mixture compositions are given in Table 3. 1).

Figure 3. 7 shows the time-dependent acoustic pressure fluctuation of propagating flames under the conditions mentioned above. The parametric instability is represented by a sudden growth of acoustic pressure occurs after the primary acoustic instability. Only a truncated pressure history until the transition to parametric instability is shown in Fig. 3. 7 to highlight the transition to parametric instability. In Fig. 3. 7, parametric instability occurs at an almost similar acoustic pressure amplitude, which is approximately $0.4\ kPa$ for all transition conditions. On the other hand, for $S_L = 13\ cm/s$, a laser power of 7 W cannot induce the transition in the case of *DLI* as the acoustic pressure in the tube does not reach $0.4\ kPa$, but the laser irradiation effect is evident in the increased acoustic pressure

compared to the case without laser irradiation for the same $S_L = 13\ cm/s$ (0W). Hence, it is confirmed that the acoustic pressure needs to reach a critical value ($0.4\ kPa$ in this experiment) to generate a transition to parametric instability, as can be seen in the stability diagram in Fig. 3. 6. In addition, the wavenumber of the corrugated structure found at the moment of the transition conditions in Fig. 3. 7 is the same as that found in Fig. 3. 6, $k = 14.1\ cm^{-1}$. This value is close to the one found in [19] and can be theoretically calculated using the presented method in their work.

Notably, the propagating flat flame at $S_L = 13\ cm/s$ without laser irradiation could not transition to parametric instability, as is evident from the pressure history shown in Fig. 3. 7. However, when the circular portion(s) of the flat flame is modified to concave segment(s) (the wavelength of the concave structure is the diameter of the circular portion) using laser irradiation, the transition could occur. This means the structural modification of the flame can trigger the emergence of the corrugated structure on the way to generate the transition (the area increase caused by the increase in tube diameter will not be effective in causing the transition as it changes acoustic losses as well as the initial growth rate of primary instability). However, a precise understanding of the relationship between laser-induced flame structures and the criteria of the transition is still obscure. This relationship can be clarified by investigating how the deformed flame in the case of *DLI* is more effective in deriving the transition than that in *SLI*.

To address this, we investigated the velocity coupling mechanism, which was first recognized by Markstein [13] who reported the effect of flame surface area variation on the generation of thermoacoustic instability. The acoustic velocity in the tube modulates the total flame surface area fluctuation, which then modulates the heat release rate in phase with the acoustic pressure fluctuation and may lead to an enhancement in acoustic vibration [14]. Considering velocity coupling, Pelce and Rochwerger [21] performed a linear analysis for a

weak cellular flame characterized by small-amplitude sinusoidal cells, $ak \ll 1$, which is just above the planar flame stability threshold. They defined the transfer function, Tr, of the heat release rate to the acoustic velocity at the flame front to calculate the growth rate of acoustic instability driven by the effect of acoustic acceleration on the geometry of the flame front. The growth rate of the instability is given by [21]:

$$1/\tau = Im(Tr)G(r, \omega_n) \tag{3.10}$$

where $Im(Tr)$ is the imaginary part of Tr and $G(r, \omega_n)$ is the acoustic structure function of the relative flame position, r, of the flame in the tube and the resonant frequencies ω_n. $G(r, \omega_n)$ represents the normalized product of the acoustic pressure times the acoustic velocity at the flame front. In this analysis, they showed that the dimension of the cellular structure of the flame is an important factor in determining the growth of the instability. Tr was found to be proportional to $(ak)^2$; thus, the growth rate of the instability is proportional to $(ak)^2$. Clanet [28] extended the calculations performed by Pelce and Rochwerger and extrapolated them to an experimental configuration of nonlinear cells far from the planar flame stability limit. With the typical aspect ratio of the wrinkling, $ak \approx 0.5$, the growth rate of thermo-acoustic instability predicted from the modified model agreed well with the experimental results of the gaseous flame (within a factor of 2).

The flame surface area in our work is controlled by laser irradiation; thus, we investigated the relation between $(ak)^2$ of the concave structure and the growth rate of the corresponding acoustic pressure fluctuation during the propagation period of the deformed concave flame at $S_L = 13\ cm/s$. The growth rate is calculated by fitting pressure time series as follows:

$$A = A_0 e^{t/\tau} \tag{3.11}$$

where $1/\tau$ is the growth rate, A_0 and A are the initial and final amplitudes of acoustic pressures, and *t* is the calculation time, which is defined from flame propagation videos and corresponds mostly to the relative stabilization period of primary acoustic instability. Precisely, the period starts from the moment after the initial growth period of primary acoustic instability (where the concave structure is fully developed) and ends with the appearance of the corrugated structure before transitioning to parametric instability. For instance, the calculated period denoted by $t_{concave}$ is shown in pressure history for $S_L = 13\ cm/s$ with *SLI* –11 W (see Fig. 3. 7).

Figure 3. 8 shows the variation in growth rate during concave structure propagation with its geometric factor $(ak)^2$. The measurements of *a* and *k* were performed, assuming that the concave structure is the sinusoidal function of *a* and λ, as shown in the upper left corner of the figure. Flame propagation videos showed that after the concave structure was fully formed, k of the concave structure was almost constant during flame propagation. On the other hand, a of the concave structure fluctuated between the maximum and minimum in each cycle of flame oscillation. Accordingly, the horizontal axis in Fig. 3. 8 presents $(ak)^2$ taken from the constant k and the averaged a taken from the maximum and minimum a. Moreover, $(ak)^2$ for *DLI* was calculated as the sum of the values for each cell of the double concave structure since each cell contributes to the total growth rate of the instability.

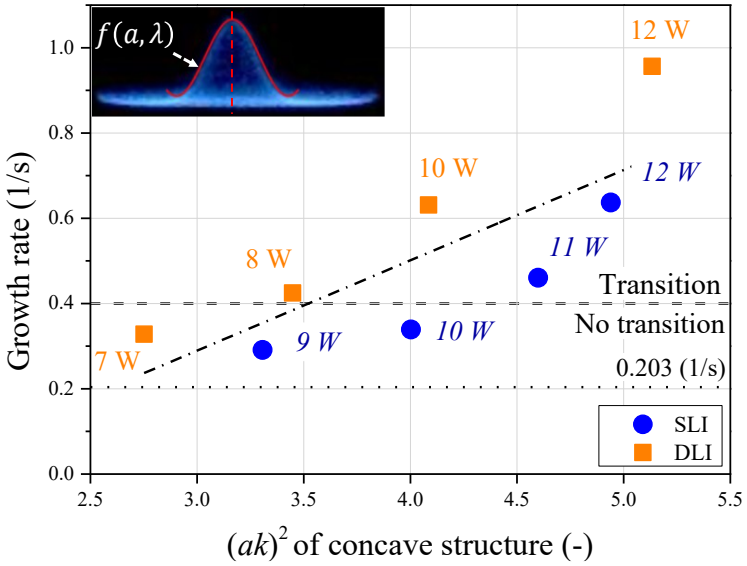

Fig. 3. 8. Relationship between $(ak)^2$ of the concave structure and the growth rate of acoustic pressure fluctuation at $S_L = 13\ cm/s$ and $Le = 1.05$. The horizontal dotted line denotes the growth rate without laser irradiation. The horizontal dashed line denotes the critical growth rate $(\sim 0.400\ 1/s)$ to reach parametric instability.

It can be seen from Fig. 3. 8 that the growth rate can be considered as a linear function of $(ak)^2$ if either *SLI* or *DLI* is considered separately. However, when both *SLI* and *DLI* experimental data are considered, an apparent discrepancy on the linear relationship between $(ak)^2$ and the growth rate can be observed. Hence, in the present experiment, the coupling $(ak)^2$ is not the criteria controlling the transition to parametric instability. The difference between this experimental result and the theoretical velocity coupling mechanism may be because cellular structures are assumed to be uniformly distributed over the flame front in the analysis of velocity coupling, while they are nonuniformly distributed and are limited in cell number in the experiments. Moreover, the velocity coupling was originally derived from a linear theory applied for a weakly cellular flame in the limit of the aspect ratio $ak \ll 1$ [21]. This linear analysis was developed to apply for the case real flame, and it was consistent

with the experimental results with a higher aspect ratio of cellular flame, $ak \approx 0.5$ [28]. On the other hand, the aspect ratio, $ak \geq 1.1$ obtained in the present work is larger than that with $ak \approx 0.5$ in the previous works [28]. Thus, with the aspect ratio, $ak \geq 1.1$, the geometric parameters of the cellular flame become very large that is in a nonlinear range where the linear analysis of velocity coupling could not be applied. Consequently, Application limit of $(ak)^2$ exists between aspect ratio ak of 0.5 and 1.1.

3.3 Mechanism to enhance instability of laser-induced flame propagating under *SLI* and *DLI*

The conversion to the concave segment(s) from the circular portion(s) of the flat flame induced by laser irradiation increased the flame surface area. This increment could be attributed to the transition to parametric instability of the flame. Hence, to clarify the effect on the increase of the flame surface area, the correlation between the concave segment area and the growth rate of acoustic pressure was investigated. Only the area of the concave structure is considered because the planar segment of the deformed flame would limit any additional contribution to derive the transition.

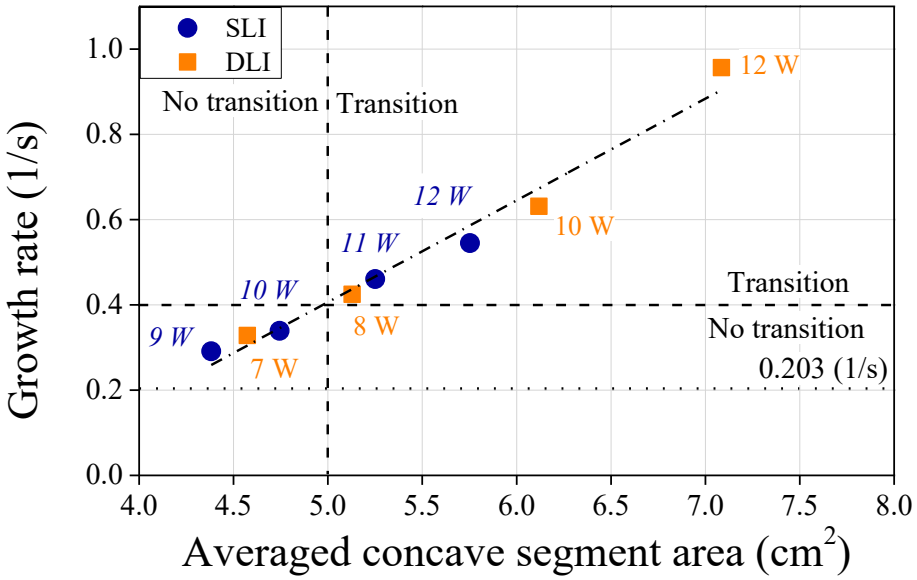

Fig. 3. 9. Relationship between the concave segment area and the growth rate of acoustic pressure fluctuation at $S_L = 13\ cm/s$ and $Le = 1.05$. The horizontal dotted line denotes the growth rate without laser irradiation. The horizontal dashed line denotes the critical growth rate ($\sim 0.400\ 1/s$) and critical average concave segment area ($\sim 5\ cm^2$), respectively to reach parametric instability.

Figure 3. 9 shows the variation in the growth rate of acoustic pressure with the measured average concave segment area. The horizontal axis presents the average area taken from the maximum and minimum areas of the concave segment during flame propagation. The growth rate of the propagating flat flame without laser irradiation at $S_L = 13\ cm/s$ was $0.203\ (1/s)$ as shown by a dotted horizontal line in Figs. 3. 8 and 3. 9; thus, the growth rate increases with laser irradiation. From Fig. 3. 9, we found that a linear relationship exists between the concave segment area and the growth rate of the acoustic pressure, indicating that an increase in the flame area causes a linear increase in the growth rate of pressure fluctuation. Thus, a larger growth rate means a higher potential for pressure fluctuation amplitude to reach the critical value of $0.4\ kPa$ to generate the transition. The growth rate

in Figs. 3.8 and 3. 9 are nearly an order of magnitude smaller than typical velocity coupling predictions [28] because the flame is in the flat flame region, as illustrated in Fig. 3. 6, where area fluctuation is suppressed due to the stability of a planar flame front. Recall that the transition of flames at $S_L = 13\ cm/s$ occurs at laser powers of 11 W and 8 W for *SLI* and *DLI*, respectively. Therefore, the graph in Fig. 3. 9 is separated into transition region and no-transition region with a threshold growth rate for the transition to parametric instability of $\sim 0.400\ 1/s$ and a corresponding concave segment area threshold of $\sim 5\ cm^2$. Next, compared to *SLI* at the same laser power, *DLI* developed a larger concave segment area corresponding to a greater growth rate of pressure fluctuation, so the flames under *DLI* need a smaller laser power to meet the transition criteria. This is why *DLI* is more effective than *SLI* in initiating the transition to parametric instability.

Notice that, the generation of convex structure deformed the flame a larger area than the generation of concave structure, this can be visualized in Fig 3. 2. However, the convex structure could not initiate the transition as concave structure did, while the flame surface area is found to be the factor linearly correlating to the growth rate of acoustic pressure. Looking back to Fig 3. 1, the corresponding flame velocity for D-L hydrodynamic instability is at $S_L = 10\ cm/s$. It is observed that the flame is weakly cellular and therefore weakly unstable of the instability since the corresponding growth rate is proportional to $(ak)^2$ as described in velocity coupling. In this case damping effects dominate and no acoustic sound is produced. For a larger S_L, e.g., flame in regime II, the flame shape modulation is of larger amplitude and destabilizing effect can overcome the damping effects. It is studied that the strength of the destabilizing effect varies as a function of the relative position in the tube [21,25]. Fig 3. 10 shows the theoretical growth rate as a function of relative flame position, r in the tube computed in [25]. Considering the case $L = 70.2\ cm$ which is almost similar to the tube length in the current experiment, the generation of convex structure is near the

open end of the tube from $0{,}8r\ to\ 0.72r$ in average. That why the amplitude of acoustic pressure fluctuation or the growth of acoustic energy in this region of the tube is not strong comparing to that in the middle of the tube where the propagation of concave structure is observed. This could be attributed to the reason that in the current experiment even induced larger flame surface area, but convex structure could not generate the transition comparing to concave structure.

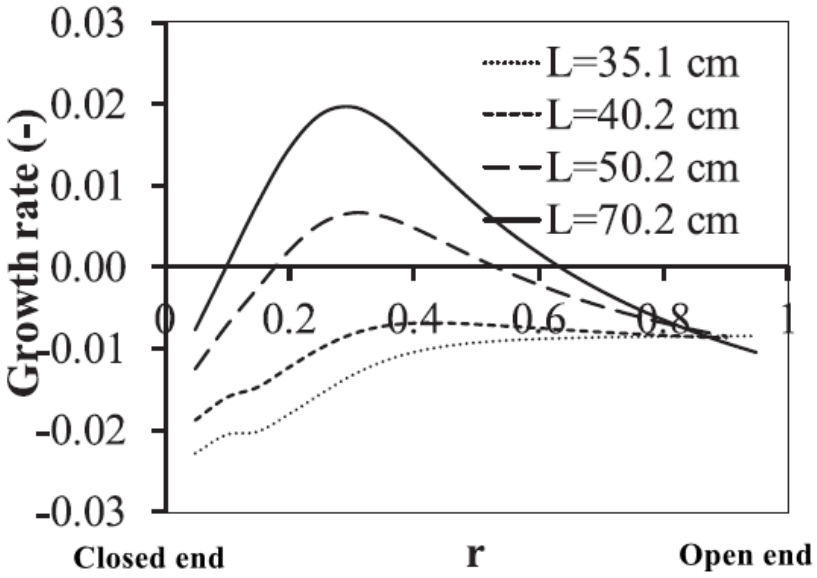

Fig. 3. 10. Theoretical growth rates along the position in the tube for various lengths, L of the tube at $S_L = 15\ cm/s$ and $D = 5\ cm$ [25].

An experiment was conducted that aims to form a convex structure at the middle of the tube to examine if the generation to parametric can be proceeded. Fig 3. 11 shows the time-dependent of acoustic pressure of the experiment. The laser is started after ignition $1.8\ s$ where the flame structure is completely planar under saturated period of primary acoustic instability. It can be seen in Fig 3. 11, the deformation of convex structure initiate at $1.86\ s$ (at around $0.5r$ in Fig 3. 10) where the acoustic pressure also starts to increase. When the acoustic pressure reaches $0.4\ kPa$ at $1.995\ s$, the transition occurs. The convex area in this

experiment is larger than the area threshold for the transition 5 cm^2. It is understood that when the convex structure is moved to the middle of the tube and meets the criteria for the transition, the transition consequently occurs. Therefore, this experiment can confirm the reliability of the above explanation accompanied with Fig 3. 10.

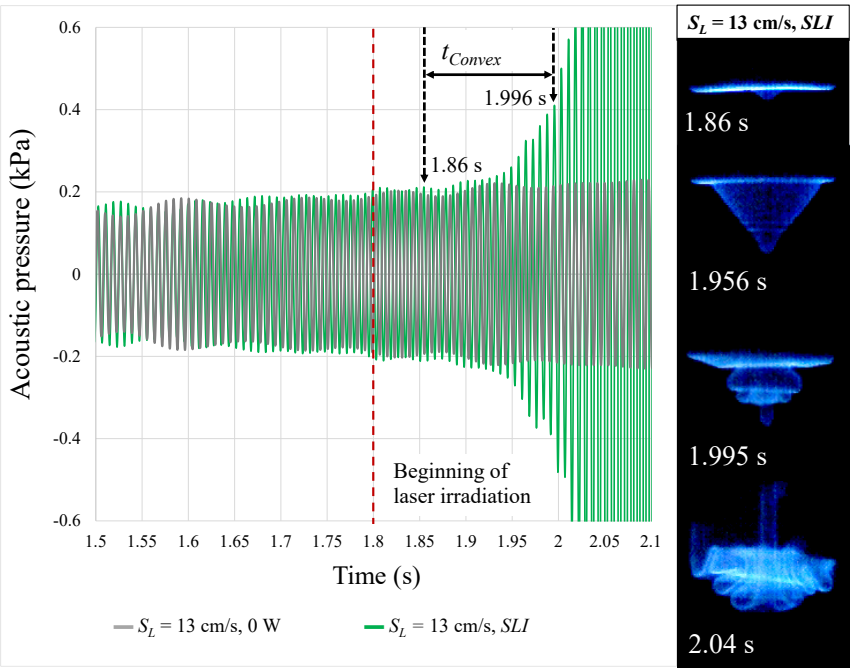

Fig. 3. 11. Time-dependent of acoustic pressure of the condition at $S_L = 13\ cm/s$ with SLI, laser starting time at 1.8 s.

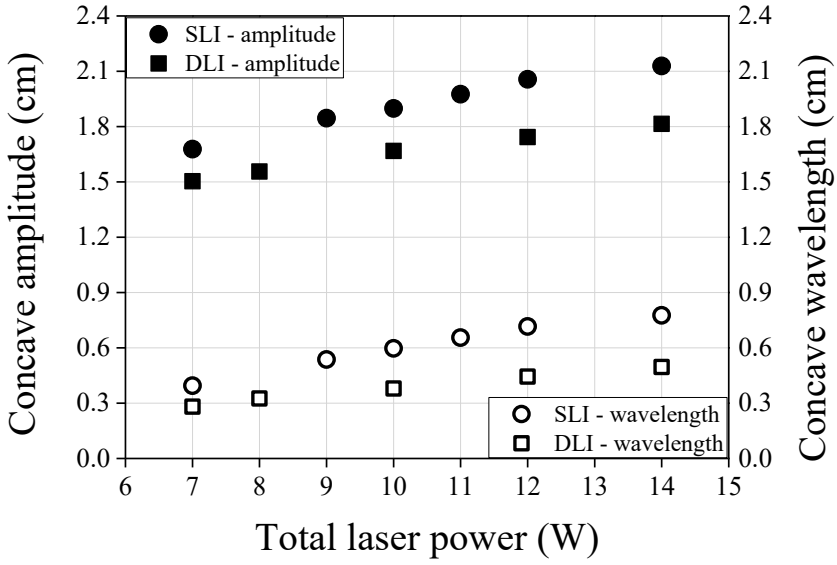

Fig. 3. 12. Amplitude and wavelength of concave structures induced by *SLI* and *DLI* at $S_L = 13\ cm/s$.

The concave segment area of the deformed flame in Fig. 3. 9 relies on a and λ of the concave structure. Subsequently, its area is calculated using the surface of revolution method. Figure 3. 10 shows the average values of a and λ of concave structures induced by *SLI* and *DLI* at $S_L = 13\ cm/s$. Under the same total laser power supply, the total power of *SLI* is twice that of the individual laser beam of *DLI*. However, the experimental results show that both a and λ of the deformed concave structure induced by *DLI* are larger than half of those induced by *SLI*, as shown in Fig. 3. 12. Thus, a larger area is deformed by *DLI* than that by *SLI* and could be the reason *DLI* is more efficient than *SLI* in inducing the transition to parametric instability.

In an earlier work [35], the laser-induced flame could generate the transition in a structure (either concave or convex) depending on whether Le is larger or smaller than unity, respectively. To clarify the reliability of the above discussion on the importance of the

deformed area on the transition criteria, additional experiments were conducted for a gas mixture with $Le = 0.8$ at $S_L = 12\ cm/s$ (mixture composition is shown in Table 3. 2).

Table 3. 2. Composition and properties of experimental gas mixtures with $Le < 1$.

C_2H_4 [%]	O_2 [%]	CO_2 [%]	ϕ	Le	S_L[cm/s]
7.780	19.447	72.773	1.2	0.8	12

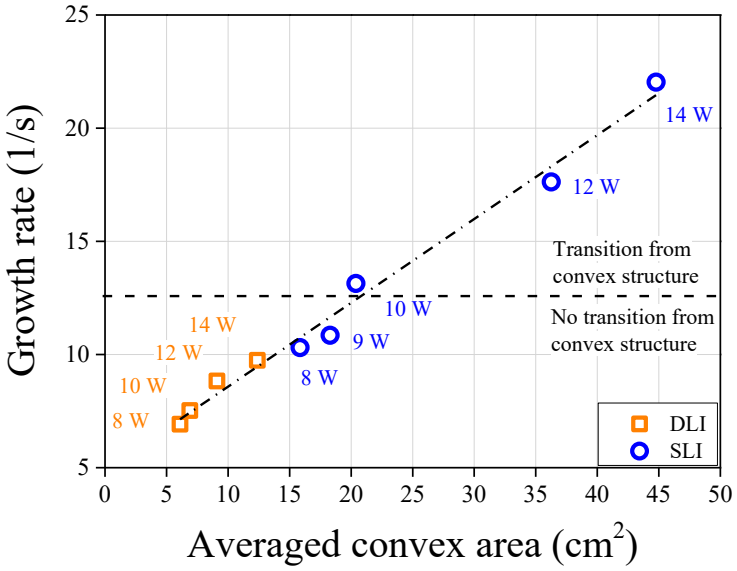

Fig. 3. 13. Relationship between the deformed convex area and the growth rate of acoustic pressure fluctuation at $S_L = 12\ cm/s$ and $Le = 0.8$.

In this low- Le experiment, the transition to parametric instability occurred only from the deformed convex structure induced via *SLI*. Interestingly, *DLI*, which was more effective than *SLI* in causing instability for the flame with $Le > 1$, was not effective for the flame with $Le < 1$. Figure 3. 13 shows the correlation between the area of the convex structure and the growth rate of acoustic pressure fluctuation during the structure's propagation period. The growth rate is calculated using Eq. (3.2) with t starting from the emerging moment of the convex structure until the structure reaches the maximum elongation (noted as t_{convex} in Fig. 3. 14). An example is shown at 10 W under *SLI* in Fig. 3. 14. The average area of the

convex structure, $\bar{S}$, during the calculated period is shown in the horizontal axis of Fig. 3. 13 and is calculated as follows:

$$\bar{S} = \frac{1}{t}\int_0^t S dt \tag{3.12}$$

Similar to the case for $Le > 1$ (Fig. 3. 9), a linear relationship between the convex area induced by *SLI* and *DLI* and the growth rate is found for $Le < 1$ (Fig. 3. 13). Figure 3. 13 shows that the double convex structures induced by *DLI* have smaller areas than single convex structures induced by *SLI* at the same total laser power. Moreover, only the deformed convex structures under *SLI* with a total laser power of more than 10 W can generate the transition. Here, the threshold growth rate and the convex area were approximately 13 $1/s$ and 20 cm^2 , respectively.

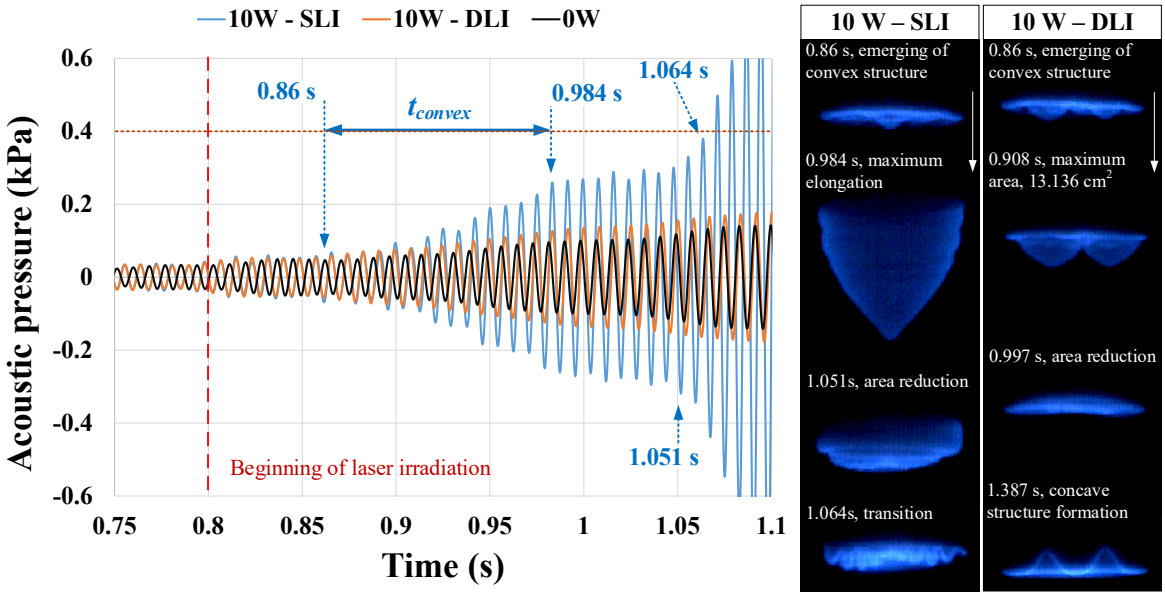

Fig. 3. 14. Comparison of the growth of the acoustic pressure fluctuation under no laser, *SLI*, and *DLI* for $S_L = 12\ cm/s$ and $Le = 0.8$.

Figure 3. 14 shows that the increasing convex area during t_{convex} for 10 W under *SLI* enhances the growth of acoustic pressure fluctuation, which further generates the transition

at a laser power of 10 W under *SLI*. As a comparison, two other cases shown in Fig. 3. 14 (10 W – *DLI* and 0 W) did not have a larger convex area and consequently a larger pressure growth that can induce instability. Moreover, for the condition of 10 W – *DLI*, the convex structure, after reaching a maximum area, is gradually diminished, and the concave structure is subsequently developed. It is noticed that the elongation of laser-induced flame tip or the increasing in size of the deformed structure is not a linear function of laser power, see Fig. 3.12 and as figured out in Ref [38], it is kind of exponential correlation with possible slope. Therefore, when a single laser power is halved like this experiment, the development of single convex structure is much stronger than the double concave structure in the tip elongation. Accordingly, *SLI* is more effective than *DLI* in deriving transition from the convex structure with $Le < 1$. Hence, area modification caused by laser irradiation is the determining factor for the generation of parametric instability.

3.4 Conclusion

The existing *SLI* setup is modified to establish a new *DLI* approach that can form double cellular structures, while *SLI* only forms single cellular structures. The experiment presented in this chapter is conducted with the objective to analyze the effect geometric structure of cellular flame on the transition from primary acoustic instability to parametric instability. With a wider range of a and k induced from both *SLI* and *DLI* experiments, it also attempted to provide an experimental validation for velocity coupling. A comprehensive criterion of the transition from primary acoustic instability to parametric instability was investigated under these two laser irradiation conditions. The results showed that the growth rate of primary acoustic instability during the propagation of the deformed flame is important to enhance the pressure fluctuation amplitude that further reaches the critical value for the transition to parametric instability. More importantly, $(ak)^2$ of the cell deformed on the flame does not provide a comprehensive transition criterion in this experiment, as mentioned

in the original theory of velocity coupling. Possibly, $(ak)^2$ does not always represent the increase in flame area due to the nonuniform deformation of the flame structure, especially when the aspect ratio, ak obtained in a nonlinear range; thus, it cannot be correlated with the growth rate across both *SLI* and *DLI* experiments. On the other hand, the measured flame area correlated well with the growth rates. Using the *DLI* method, we proved that the actual flame area, rather than $(ak)^2$, determines the growth rate under nonhomogeneous cell distribution. Moreover, application limit of the coupling $(ak)^2$ exists between aspect ratio ak of 0.5 and 1.1.

Chapter 4: Effect of flames induced by DLI in variation of beam separated distance on the thermo-acoustic instability

This chapter attempts to present an experimental investigation on *DLI* experiment with different distances between two laser beams. The beam separated distance was varied from a narrow distance where two cellular structure induced by two laser beams of *DLI* are merged together to a possible widest distance where that two cells are completely far from each other. When two cells are merged at the narrow distance of beam separation as they superimpose to each other, the shape of whole double cell is no longer a sinusoidal one. At wider distances of beam separation where one cell does not touch another one, the sinusoidal shape is kept for each cell. The aim of this experiment is creating different geometric deformed shape of the double cellular structure using *DLI* setup at a constant laser power and laminar burning velocity. Notice that, the deformed structures when flame exposed to *SLI* and *DLI* presented in Chapter 3 are induced as sinusoidal shapes only and the beam separated distance is fixed in *DLI* setup. The experiment was conducted with an objective to examine the effect of different geometric structure (sinusoidal and non-sinusoidal shape) of flame induced by *DLI* on the growth rate of thermo-acoustic instability.

4.1. Experimental setup and procedure

This experiment was conducted using the *DLI* setup presented in Chapter 3. The beam separated distance, S_b, varies from 12 mm to 21 mm with 3 mm interval. The corresponding arrangements of the double beams are shown in Fig. 4. 1. The figure shows the variation of beam separated distances of *DLI* setup at the top view of the top lid as shown in Fig. 2. 1. The position of the laser beams was set symmetrically around the center point of the ZnSe window. This results in a regular distribution of cellular structures induced by *DLI* respected to the center line of the tube. Notice that, before conducting experiment, the power of laser

beams from *DLI* at various beam separated distances was measured carefully to ensure comparability for the results of the experiments.

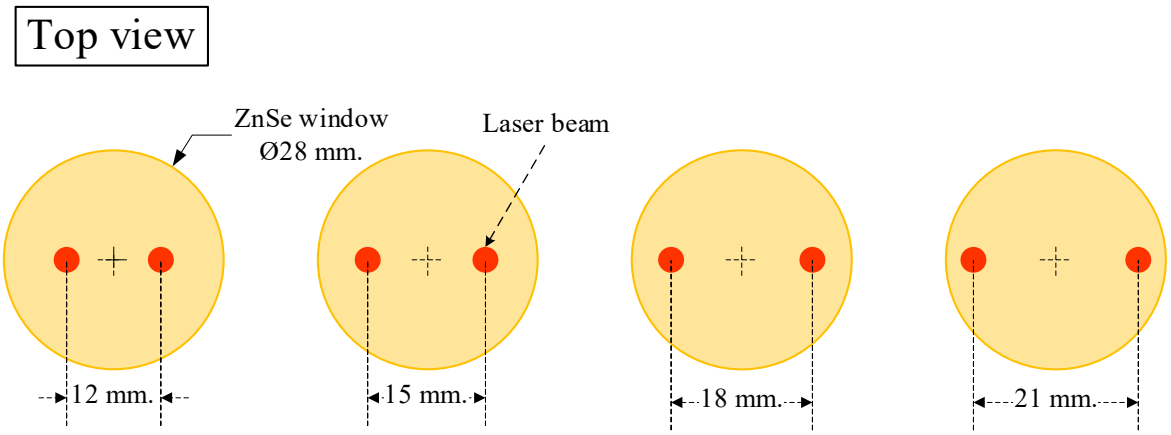

Fig. 4. 1. Arrangement of *DLI* with variation of beam separated distance.

In general, the procedure is similar to the experiment shown in Chapter 3. The experiment was carried out with mixture of $C_2H_4/O_2/CO_2$ at $Le = 1.05$ and laminar burning velocity, $S_L = 13\ cm/s$. Table 3. 1 lists the properties and compositions of the gas mixture. Starting of laser is set at $0.8\ s$ after the ignition. The laser exposure of flames is continuous for 3 s. The constant laser power at $7\ W$ was chosen in the experiment. According to Fig. 3. 5, the flames at $S_L = 13\ cm/s$ and $7\ W$ of *DLI* was not able to generate the transition. Therefore, the propagation period of concave structures was mainly focused. Note that the experiment at the beam separated distance, $S_b = 18\ mm$, which is the same with the one as presented in Chapter 3, was repeated in the series of experiments with variation of S_b. In addition, the experiment at $7\ W$ under *SLI* was also conducted for further comparison. This experimental condition was assumed as the one with $S_b = 0\ mm$.

4.2. Observation of downward-propagating flame induced by *DLI* with various beam separated distances.

Figure 4. 2 shows the front-side view of downward-propagating flames at various beam separated distances, S_b . It is familiar with the double concave structure at $S_b = 0\ mm, 18\ mm$ and $21\ mm$ as they appeared in sinusoidal shapes which were already observed in the previous experiments shown in chapter 3. On the other hand, the double concave structures resulted from experiments at $S_b = 12\ mm$ and $15\ mm$ were different from the others. In fact, two individual concave cells superimposed and the resulted an overlapping region between them and it is moved upwardly from the flame base. Consequently, these structures were no longer in a sinusoidal shape. The typical time-dependent of acoustic pressure recorded during flame propagation in the experiments are shown in Fig. 4. 3. The acoustic pressure profile of these condition are quite similar. A further investigation on the effect of concave structures obtained from the experiment shown in Fig. 4. 2 on the growth rate of the thermo-acoustic instability is discussed in next section.

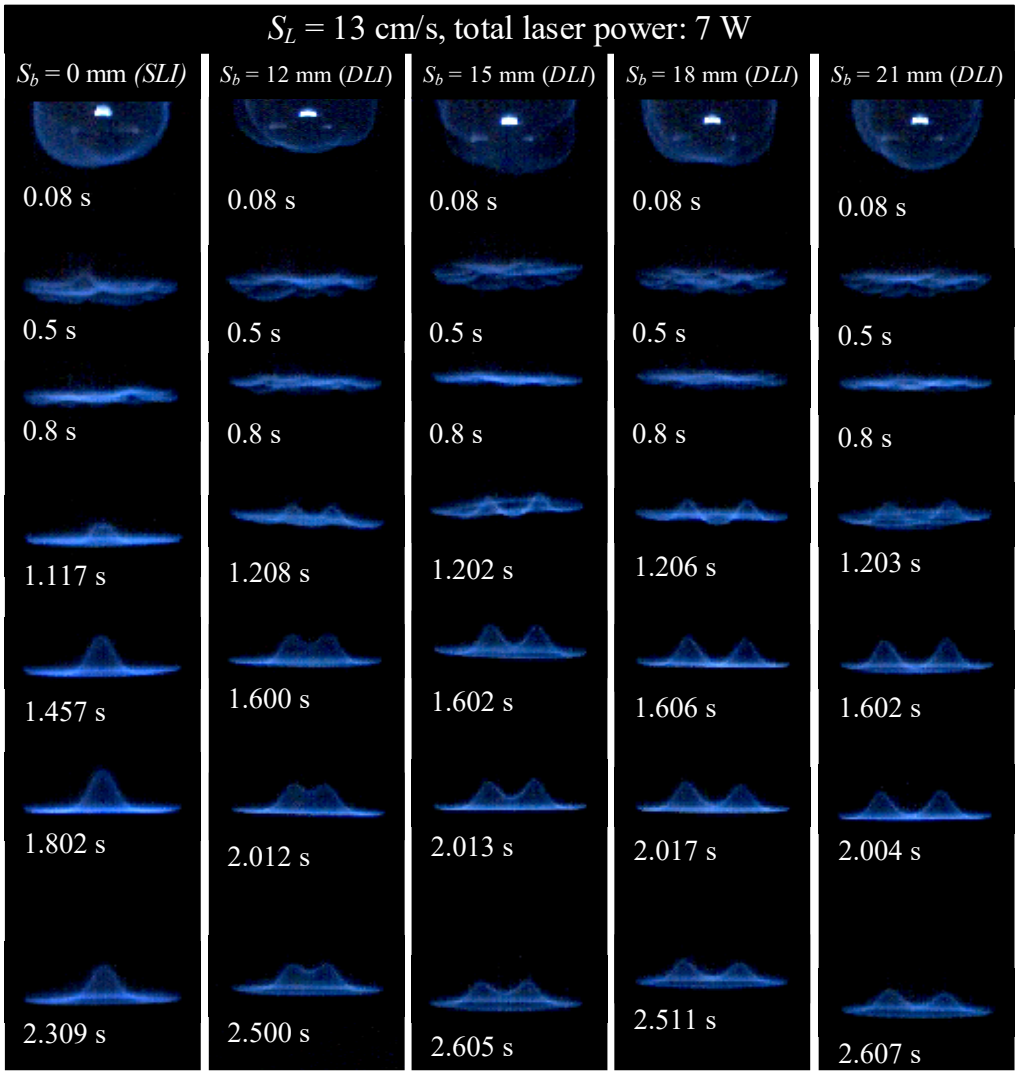

Fig. 4. 2. Still images of typical downward-propagating flame exposing to laser irradiation in variation of beam separated distances (mixture compositions are given in Table 3. 1).

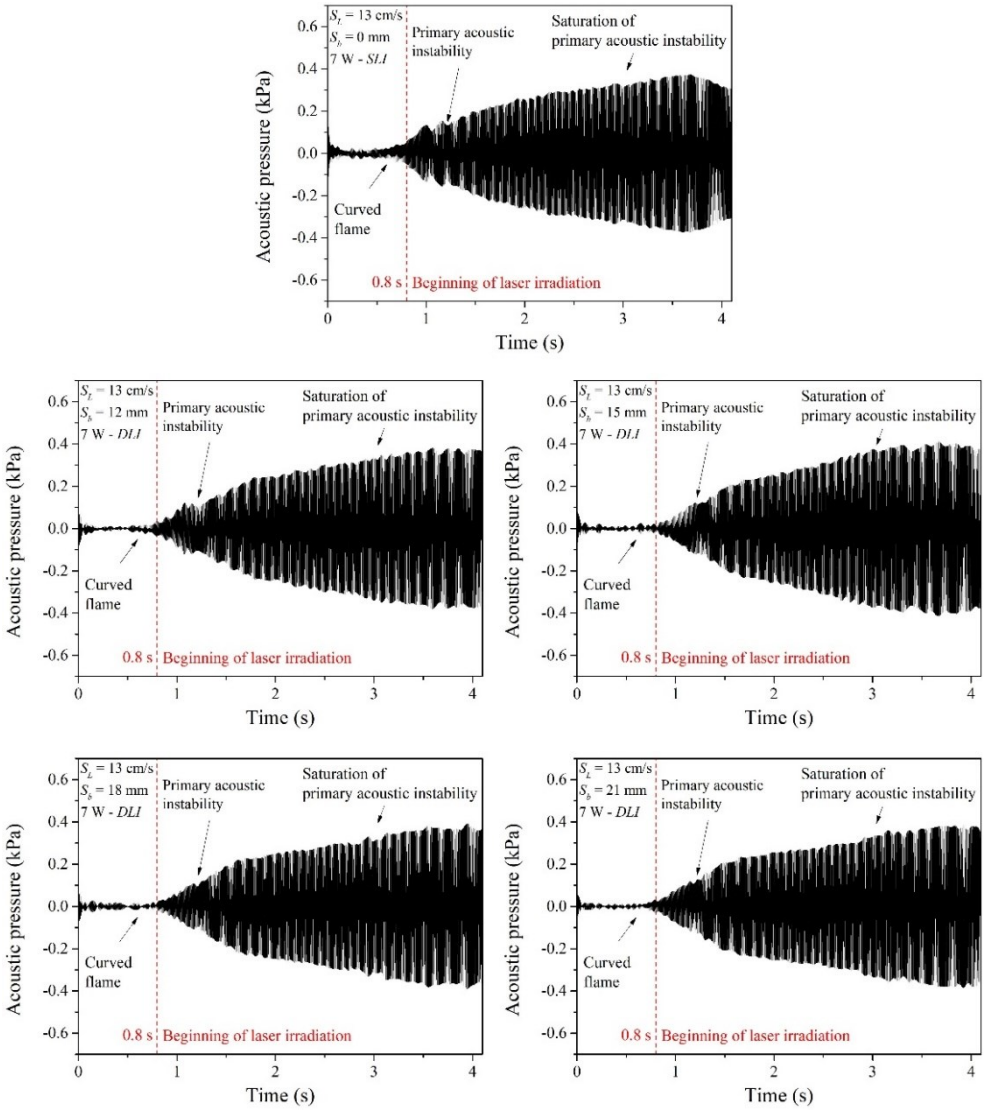

Fig. 4. 3. Acoustic pressure fluctuations of the conditions shown in Fig. 4. 2.

4.3. The effect of concave structures induced from different beam separated distance on the growth rate of thermo-acoustic instability

The correlation between concave segment area and the corresponding growth rate of acoustic pressure during the structure propagation is discussed in this section. The area of double concave segments induced at narrow beam separated distances, $S_b = 12\ mm$ and $15\ mm$ were carefully examined. Along with the front-side view, an additional left view was recorded as an attempt to define these concave structures. Fig. 4. 4 shows still images of the

concave structure at $S_b = 12\ mm$ and 7 W. In Fig. 4. 4, the left view image shows that there is no deformation including the overlapping region that is distorted exceeding the boundary profile of the concave structures. A similarity was observed for the concave structure at $S_b = 12\ mm$, and 7 $W - DLI$. Accordingly, with some assumptions, these concave structures are described as follow.

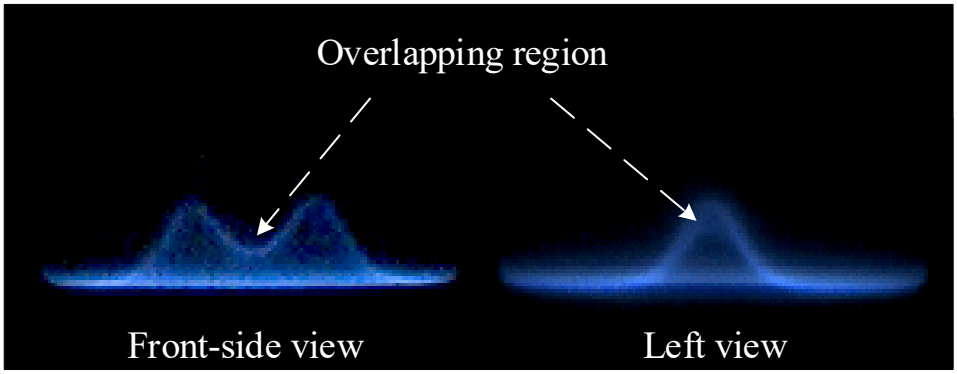

Fig. 4. 4. Still image of the concave structure taken at $S_b = 15\ mm$ and 7 $W - DLI$.

At first, the boundary profile of each concave structure was defined. Fig. 4. 5 illustrates geometric definitions of concave structures at $S_b = 12\ mm$ and 15 mm with 7 $W - DLI$. They were constructed from a part of two sinusoidal concave cells, called cell 1 and cell 2. They are mathematical given as a sine function:

$$y = a\sin\left(\frac{2\pi x - \varphi}{\lambda}\right) \tag{4.1}$$

where a, ϕ and λ are the amplitude, phase and wavelength of geometry of the cell.

For the overlapping region, the boundary profile at the side-view of the region was assumed as it is given by a summation of the functions describing the two concave cells:

$$\begin{aligned} y_1 + y_2 &= a_1\sin\left(\frac{2\pi x - \varphi_1}{\lambda_1}\right) + a_2\sin\left(\frac{2\pi x - \varphi_2}{\lambda_2}\right) \\ &= (a_1 - a_2)\sin\left(\tfrac{2\pi x - \varphi_1}{\lambda_1}\right) + 2a_2\sin\left[\left(\tfrac{1}{\lambda_1} + \tfrac{1}{\lambda_2}\right)\pi x - \tfrac{1}{2}\left(\tfrac{\varphi_1}{\lambda_1} + \tfrac{\varphi_2}{\lambda_2}\right)\right]\cos\left[\left(\tfrac{1}{\lambda_1} - \tfrac{1}{\lambda_2}\right)\pi x - \tfrac{1}{2}\left(\tfrac{\varphi_1}{\lambda_1} - \tfrac{\varphi_2}{\lambda_2}\right)\right] \end{aligned} \tag{4.2}$$

After that, the summation function was examined and showed a well-fitting to the boundary profile at the overlapping region, see Fig. 4. 5. Then this assumption was used in constructing the double concave structure.

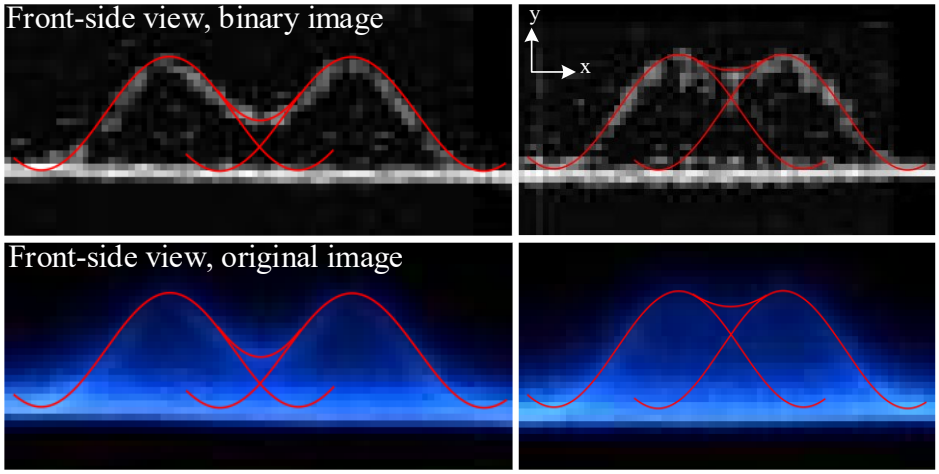

Fig. 4. 5. Edge boundary of concave structures at $S_b = 12\ mm$ and $15\ mm$ with $7\ W - DLI$.

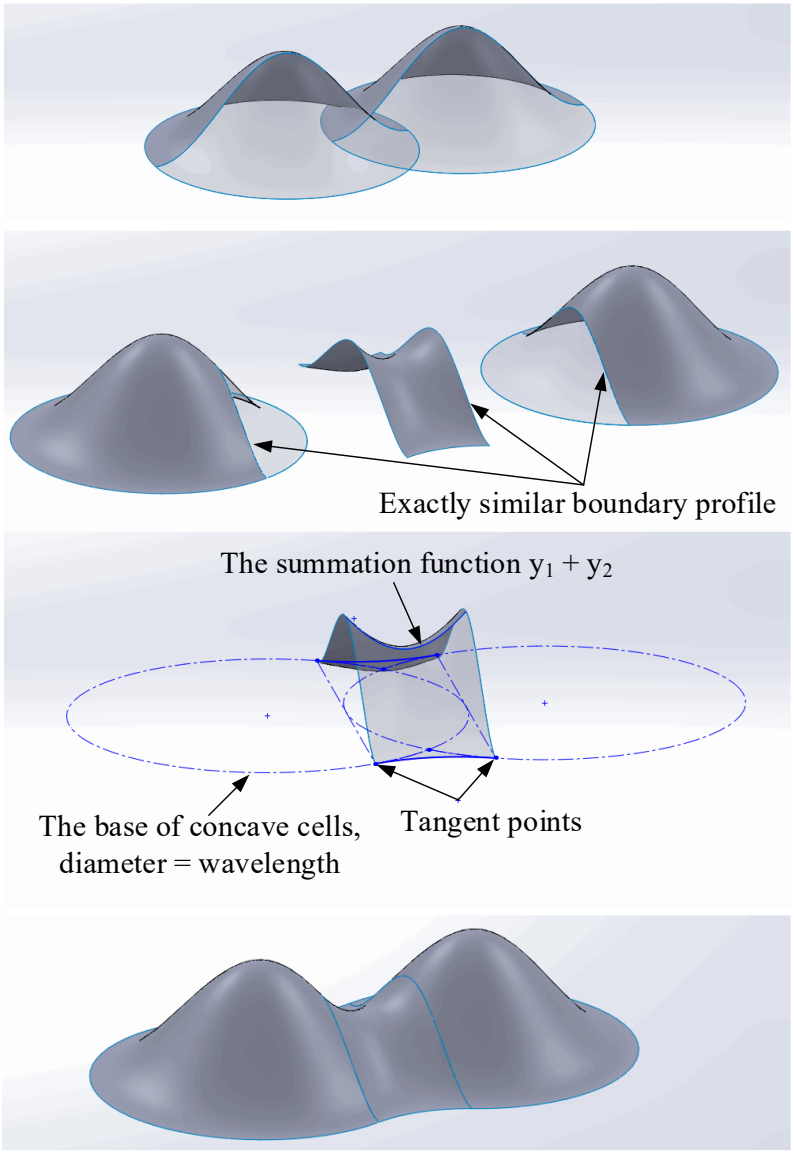

Fig. 4. 6. The construction of double concave structure at $S_b = 15\ mm$ with 7 $W - DLI$.

Figure 4. 6 shows a 3D construction of the double concave structure at $S_b = 15\ mm$ with 7 $W - DLI$. It was assumed that the structure is formed by cutting two concave cells at the overlapping region by planes at a direction that normal to the flame base and replacing that region by a tangent surface. The tangent surface is created based on the summation function (calculated from Eq. 4. 2) with a constraint is that after it is ensembled with the remain part of two concave cells, an entire smooth surface is formed as shown in the bottom image in Fig. 4. 6. This way of construction for the concave structure at $S_b = 15\ mm$ was

similar to that at $S_b = 12\ mm$. Eventually, the area of the concave segments could be measured. For other $S_b = 0\ mm, 18\ mm$ and $21\ mm$, the concave structures were also defined based on Eq. 4. 1 and the concave segment area were taken using the method of revolution as the same way of that done in previous chapter.

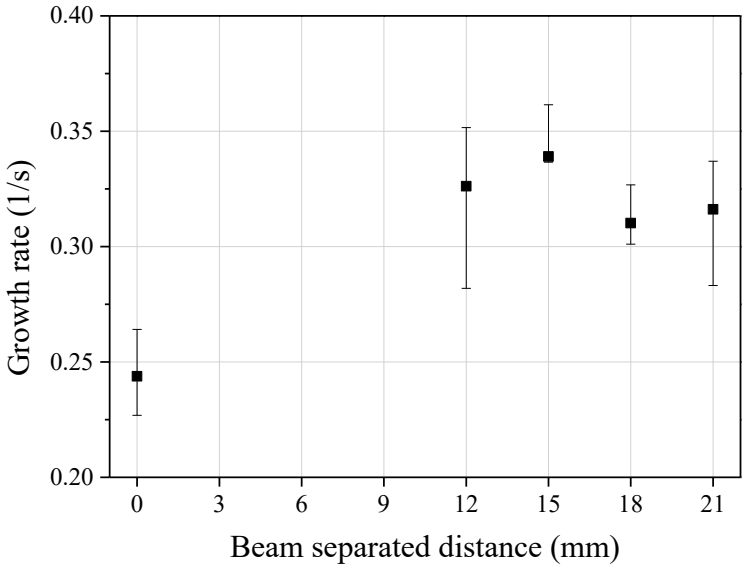

Fig. 4. 7. Growth rate of acoustic pressure fluctuation at $S_L = 13\ cm/s, 7\ W$ in variation of beam separated distance, S_b.

Figure 4. 7 shows variation of growth rate of acoustic pressure fluctuation during propagating of concave structure as a function of beam separated distance, S_b. The growth rate is calculated using Eq. 3.2. It was known from the previous chapter that at the same total laser power, the growth rate of acoustic pressure at $S_b = 0\ mm$ (*SLI*) is smaller than that of others S_b with *DLI* as shown in Fig. 4. 7. A nearly similar growth rate can be seen between conditions of $S_b = 18\ mm$ and $21\ mm$. It is understandable as double concave structures at these two conditions are almost similar in size or area, just different in the distance between two concave cells. Among the *DLI* conditions shown in the figure, it can be seen that the highest growth rate is obtained at $S_b = 15\ mm$ and followed by the growth rate of $S_b =$

12 mm. A further analysis on the effect of the concave structures on the growth rate of thermo-acoustic instability is carried out the clarified the result shown in Fig. 4. 7.

A correlation between the concave segment area and the corresponding growth rate of acoustic pressure during the propagation of deformed concave flame is shown in Fig. 4. 8. It can be seen that the concave segment area and growth rate of acoustic pressure at wider beam separated distances, $S_b = 18\ mm$ and 21 mm are almost the same. On the other hand, even with smaller concave segment areas, the growth rate given at $S_b = 12\ mm$ and 15 mm are above the linear correlation between the concave segment area and the growth rate of acoustic pressure (including the conditions at $S_b = 0\ mm, 18\ mm$ and 21 mm) following the conclusion in Chapter 3. Therefore, there was a different effect on the growth rate of acoustic pressure caused by the sinusoidal concave structure and non-sinusoidal one.

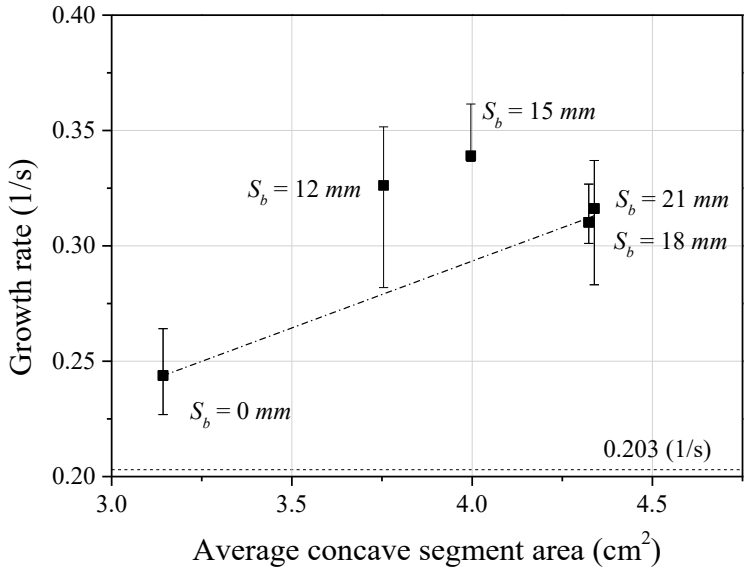

Fig. 4. 8. Relationship between the concave segment area and the growth rate of acoustic pressure fluctuation at $S_L = 13\ cm/s$, 7 W under various S_b(s). The horizontal dotted line denotes the growth rate without laser irradiation.

The difference can be attributed to the additional effect of overlapping region at narrow S_b conditions. The overlapping region is formed by a structure that the effect of the curvature is presented under $Le > 1$. Under Le is different than unity, the effect of curvature contributes to the frame front instability [42]. Therefore, it is predicted that the growth rate of acoustic pressure plotted in Fig. 4. 8 at narrow $S_b = 12\ mm$ and $15\ mm$ was total growth rate given by the effect of the concave segment area and the curvature effect of the overlapping region. The contribution on the growth rate of the concave segment area is assumed to defined following the linear relationship established from the conditions at $S_b = 0\ mm$, $18\ mm$ and $21\ mm$ as the linear fitting line shown in Fig. 4. 8. The additional growth rate is subjected to the effect of curvature presented in the overlapping region.

The contributed portion on the total growth rate of concave segment area and curvature of overlapping region were considered. Fig. 4. 9 shows the contribution on the growth rate of acoustic pressure driven by the effect of concave segment area and the effect of curvature presented in the overlapping region. The vertical axis is the ratio of the growth rate obtained from narrow conditions over the growth rate $(0.203\ 1/s)$ of the condition at the same laminar burning velocity $S_L = 13\ cm/s$, but without laser irradiation.

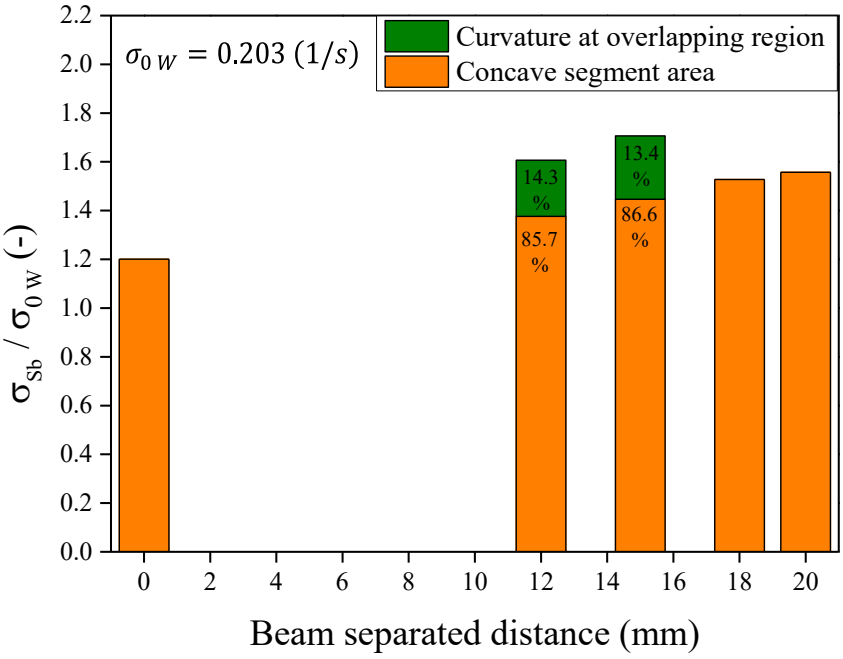

Fig. 4. 9. Contribution of the effect of concave segment area and curvature on overlapping region on the growth rate of acoustic pressure at $S_L = 13\ cm/s$ with $7\ W - DLI$.

From Fig. 4. 9, it can be seen that the contribution of the curvature effect at the overlapping region is much smaller than that of the effect of concave segment area. In fact, a quantitative comparison between the growth rate of acoustic pressure at narrow and wider S_b revealed that the deviation between them was little that may be due to the limited effect of curvature at the overlapping region as shown in Fig. 4. 9. It can be seen clearer in Fig 4. 9, when increasing S_b from $12\ mm$ to $15\ mm$, the contribution of the curvature effect on the total growth rate of acoustic pressure decreases as increasing the concave segment area. Moreover, the contribution on the growth rate of curvature effect of the overlapping region could not help the flame generating the transition where the critical laser power for the transition at $S_L = 13\ cm/s$ using *DLI* is $8\ W$ as clarified in Fig. 3. 5. Comparing the growth rate of acoustic pressure at $S_b = 12\ mm$ and $15\ mm$ where their structures of double concave are in similar shape, the higher growth rate is given for $S_b = 15\ mm$ as a larger area

induced. Therefore, in general, the concave segment area is still considered as a main factor controlling the growth rate of acoustic pressure during the propagation period of the concave structure.

4.4. Conclusion

This chapter presented an experiment on varying beam separated distance, S_b in *DLI* setup. The effect of the resulted concave structures was examined regarding their contribution on the growth rate of acoustic pressure. At the narrow $S_b = 12\ mm$ and $S_b = 15\ mm$ where double concave structure showed an overlapping region caused by superimposing of two concave cells, a presence of curvature effect on the overlapping region contributed to the total growth rate of acoustic pressure. A further analysis showed that this curvature effect appeared on the overlapping region has a limited contribution to the total growth rate of acoustic pressure. The concave segment area is revealed as the factor mainly controlling the growth rate. This is a finding that follows the results in previous chapter.

Chapter 5: Summary

This experimental study focused on the effect of flame deformation of downward propagating flames induced by laser irradiation method on its combustion instability. The study was carried out by experiments on setups of *SLI* and *DLI*. An optical arrangement is assembled with the existing *SLI* setup to establish a new setup for *DLI*. The *DLI* can form double cellular structures, while *SLI* just forms single cellular structures.

In Chapter 3, experiments with these two deformed structures are examined to develop a criterion of the transition from primary acoustic instability to parametric instability in laser irradiation experiments. The experimental result obtained from *SLI* and *DLI* showed an important conclusion that the deformed surface area is the factor controlling the criteria of transition to parametric instability. The results showed that the growth rate of primary acoustic instability during the propagation of the deformed flame is important to enhance the pressure fluctuation amplitude that further reaches the critical value for the transition to parametric instability. More importantly, in the non-linear range of aspect ratio, $ak \geq 1.1$, the coupling $(ak)^2$ of the nonuniform cellular flame did not provide a comprehensive transition criterion that described in the original linear theory of velocity coupling. Possibly, $(ak)^2$ does not represent the increment in flame surface area, then it cannot be correlated with the growth rate across both *SLI* and *DLI* experiments. On the other hand, the measured flame area correlated well with the growth rates. Using the *DLI* method, the actual flame surface area was proofed, rather than $(ak)^2$, to determines the growth rate under nonhomogeneous distribution of cellular flame. Therefore, the application of the coupling $(ak)^2$ limited between aspect ratio ak of 0.5 and 1.1.

In Chapter 4, The effect of the different geometric structure of double concave flame induced from *DLI* on the growth rate of acoustic pressure was clarified. The double concave

structures were deformed under various beam separated distances, S_b controlled in *DLI* setup. At the narrow range of $S_b = 12\ mm$ and $15\ mm$, the *DLI* resulted an overlapping region created by a superimposing of concave cells. As a result, a presence of curvature effect on the overlapping region was contributed to the total growth rate of acoustic pressure. A further analysis about the effect of concave structure revealed that the curvature effect appeared on the overlapping region has a limited contribution to the total growth rate. This effect weakens when a larger concave segment area is induced. In general, the results showed a consistent to the one discussed in Chapter 3 that concluded the dominance of deformed area in enhancing the growth rate of acoustic pressure.

References

[1] P. Clavin, G. Searby, Combustion Waves and Fronts in Flows, Cambridge, UK, 2016.

[2] G. Darrieus, Unpublished work presented at La Technique Moderne, and at Le Congrés de Mécanique Appliqueée (1945).

[3] L. Landau, Acta Phys. Chim., URSS 19 (1944) 77-85.

[4] J. Jarosinski, B. Veyssiere, Combustion Phenomena: Selected Mechanisms of Flame Formation, Propagation and Extinction, CRC Press, New York, 2008.

[5] C. Clanet, G. Searby, Phys. Rev. Lett. 80–17 (1998) 3867–3870.

[6] G.H. Markstein, Proc. Comb. Inst. 4 (1953) 44–59.

[7] J.-P. Hathout, (1999) 16.

[8] B. Higgins, A J. Nat. Philos. Chem. Arts 1 (1802) 131.

[9] P.L. Rijke, Philos. Mag. 17 (1859) 419–422.

[10] T.C. Lieuwen, V. Yang, Combustion Instabilities in Gas Turbine Engines: Operational Experience, Fundamental Mechanisms, and Modeling, 2006.

[11] P. Clavin, P. Pelcé, L. He, J. Fluid Mech. 216 (1990) 299–322.

[12] A.C. Mcintosh, Combust. Sci. Technol. 75 (1991) 287-309.

[13] G.H. Markstein, Proceeding Sixth Natl. Congr. Appl. Mech. (1970) 11–33.

[14] G. Searby, D. Rochwerger, J. Fluid Mech. 231 (1991) 529–543.

[15] T. Poinsot, A. Trouve, D. Veynante, S. Candel and E. Esposito., J. Fluid Mech. 177 (2006) 265–292.

[16] P. Clavin, J. Sun, Combust. Sci. Technol. 78 (1991) 265–288.

[17] T.C. Lieuwen, Y. Neumeier, and B.T. Zinn, Combust. Sci. Technol. 135 (1998) 193–211.

[18] G. Searby, Combust. Sci. Technol. (2007) 37–41.

[19] A.K. Dubey, Y. Koyama, S.H. Yoon, N. Hashimoto, O. Fujita, Combust. Flame 216 (2020) 326–337.

[20] R.A. Dunlap, Resonance of flames in a parallel-walled combustion chamber. Technical Report Project MX833, Report UMM-43, Aeronautical Research Center. University of Michigan, 1950.

[21] P. Pelce, D. Rochwerger, J. Fluid Mech. 239 (1992) 293–307.

[22] B.V. Rauschenbakh, Vibrational Combustion. Moscow: Mir. (1961).

[23] V. Vaezi, R.C. Aldredge, Combust. Flame 121 (2000) 356–366.

[24] R.C. Aldredge, N.J. Killingsworth, Combust. Flame 137 (2004) 178–197.

[25] Ajit Kumar Dubey, Y. Koyama, N. Hashimoto, O. Fujita, Proc. Combust. Inst. 37 (2019) 1869-1877.

[26] A.K. Dubey, Y. Koyama, N. Hashimoto, O. Fujita, Proc. Combust. Inst. 000 (2020) 1–10.

[27] A.K. Dubey, Y. Koyama, N. Hashimoto, O. Fujita, Combust. Flame 205 (2019) 316–326.

[28] C. Clanet, G. Searby, P. Clavin, J. Fluid Mech. 385 (1999) 157–197.

[29] S.H. Yoon, T.J. Noh, O. Fujita, Combust. Flame 170 (2016) 1–11.

[30] M. Tsuchimoto, O. Fujita, T. Honko, Y. Nakamura, H. Ito, Proc. Combust. Inst. 32 I (2009) 1003–1009.

[31] S.H. Yoon, T.J. Noh, O. Fujita, Proc. Combust. Inst. 36 (2017) 1603–1611.

[32] O.F. Sung Hwan Yoon, Longhua Hu, Combust. Flame 188 (2018) 1–4.

[33] J.S. Park, O. Fujita, Y. Nakamura, H. Ito, Proc. Combust. Inst. 33 (2011) 1105–1112.

[34] Y. Taniyama, O. Fujita, Combust. Flame 161 (2014) 1558–1565.

[35] Y. Chung, O. Fujita, N. Hashimoto, Proc. Combust. Inst. 000 (2018) 1–8.

[36] R.J. Kee, R.M. Rupley, et al., CHEMKIN PRO, Reaction Design, Inc., San Diego, CA, 2009.

[37] The National Institute of Standards and Technology (NIST), Available at http: //webbook.nist.gov/chemistry.

[38] K. Aguilar, Y. Taniyama, H. Ito, O. Fujita, Combust. Sci. Technol. 186 (2014) 1434–1446.

[39] J. Yáñez, M. Kuznetsov, R. Redlinger, Combust. Flame 160 (2013) 2009–2016.

[40] T. Jones, Mathieu's equation solution and stability, <http://www.physics.drexel.edu/~tim/open/mat/node2.html >.

[41] J.E. Sträng, https://arxiv.org/abs/math-ph/0510076v2.

[42] C.K. Law, Symp. Combust. (1989).

Achievements

Journal publications:

1. **Nguyen Truong Gia Tri**, Ajit Kumar Dubey, Nozomu Hashimoto, Osamu Fujita, Effect of flame surface area of downward propagating flames induced by single and double laser irradiation on transition to parametric instability, Combustion and Flame, Elsevier, Volume 223, pp 450-459, 2021.

Conference publications:

1. **Nguyen Truong Gia Tri**, Nozomu Hashimoto, Osamu Fujita, Effect of external acoustic wave on thermoacoustic instability of downward propagating flame, 56th Symposium (Japanese) on Combustion, Osaka, Japan, Nov, 2018.
2. **Nguyen Truong Gia Tri**, Nozomu Hashimoto, Osamu Fujita, Experimental Comparison on Transited Criteria to Parametric Instability of a Downward-propagating Flame in a Tube Induced by Single Laser Irradiation and Double Laser Irradiation, 12th Asia-Pacific Conference on Combustion, Fukuoka, Japan, July, 2019.
3. **Nguyen Truong Gia Tri**, Nozomu Hashimoto, Osamu Fujita, Experimental investigation on the transition to parametric instability of downward propagating flames induced by single and double laser irradiation, 58th Symposium (Japanese) on Combustion, Japan, Dec, 2020.